LAPPEENRANTA UNIVERSITY OF TECHNOLOGY
LUT School of Energy Systems
Mechanical Engineering

Daria Dobrina

THE STUDY OF LASER ABLATION'S FEATURES OF ALUMINOSILICATE CERAMICS

Examiners: Professor, D.Sc. (Tech.) Antti Salminen

Abstract

Lappeenranta University of Technology

LUT School of Energy Systems

LUT Mechanical engineering

Daria Dobrina

The study of laser ablation's features of aluminosilicate ceramics
Master Thesis

2018

85 pages, 68 figures, 15 tables, 30 equations

Examiners: Professor, D.Sc. (Tech.) Antti Salminen

Keywords: Laser ablation, Near IR irradiation, IR irradiation, Alumina ceramics

The Master Thesis studied the liquid-assisted laser ablation of ceramics. Six alumina ceramics materials with different composition (Al_2O_3 from 16% to 98%, SiO_2 up to 72%) were exposed to pulsed and continuous wave irradiation in near IR and IR regions. The effect of bulging of melt bath during ablation and expansion to the glass sphere above crater after cessation of laser action were observed, recorded and analyzed. The samples mostly prone to this effect were defined. In addition, thickness, hardness, chemical and optical properties of spheres were measured. The overall mechanism and modeling were presented according to high-speed camera and thermal imaging monitoring data.

Table of contents

LIST OF SYMBOLS AND ABBREVIATIONS

a	Thermal diffusivity coefficient [m^2/s]
a	Distance between interference stripes [m]
b	Shift of interference stripes [m]
c	Heat capacity [J/(kg*K)]
D_0	Diameter of beam before lenses [μm]
D_{bw}	Diameter of focal point [μm]
d	Height of specimen [m]
F	Force of viscosity [N]
f	Focal length [μm]
h	High of sphere [mm]
I	Light intensity [W/m^2]
k	Temperature conductivity [W/(m*K)]
k	Coefficient of microscope lens
L_v	Latent heat of vaporization [J/kg]
M^2	Beam quality factor
n	Refractive index
P	Power [W]
P_{air}	Air pressure [Pa]
$P_{surface\ tension}$	Surface tension pressure [Pa]
$P_{viscous\ friction}$	Viscous friction pressure [Pa]
$P_{water\ vapor}$	Water vapor pressure [Pa]
Q_a	Absorbed laser energy [J]
r	Radius [mm]

R	Rayleigh length [μm]
R	Gas constant [J/mol*K]
S	Surface area of sphere [m^2]
t	Current time [s]
T	Temperature [K]
T_0	Initial temperature [K]
T_b	Boiling temperature [K]
T_{out}	Surrounding temperature [K]
V	Velocity of liquid-vapor boundary [m/s]
V	Volume [mm^3]
x, y, z	Cartesian coordinates [m]

α	Optical absorption [m^{-1}]
Δ	Path difference [m]
η	Dynamic viscosity [Pa*s]
λ	Wavelength [μm]
v	Speed of radius increase [mm/s]
v	Mole [mol]
ρ	Material density [kg/m^3]
σ	Surface tension coefficient [N/m]

DAML	Droplet-assisted laser micro-machining
f.p.p.	Focal plane position
MEMS	Microelectromechanical systems

PLA	Pulse laser ablation

1 INTRODUCTION

Researches are motivated in investigation of laser ceramics ablation because of various ceramics application from microelectronic and high-power electronics to aerospace (Sola, Escartin, Cases & Pena 2011 p. 5413, Yang, Yu, Cui & Huang 2012, p.3643).

Ceramics might have outstanding properties such as lightness, extraordinary hardness, high thermal conductivity, high-temperature strength, high electrical resistivity, high dielectric strength, high insulation resistance, chemical inertness (chemical stability at high temperature), corrosion and wear resistance. (Li, Shi, Si, et al. 2009, 78, Sola et al. 2011, p. 5413, Samant & Dahotre 2009, p. 970, Wang, Lin, Wang et al. 2017, p. 1157) Advanced ceramics are utilized as structural components (Garcia-Giron, Sola & Pena 2016, p. 548). Some of them are considerably appealing for using as composite materials, electronics (electrical insulator), microelectromechanical systems (MEMS) and even as micro-optical components (Ramoli, Khan, Valentini 2017, p. 113). For example, Al_2O_3 has large band gap (3 ÷ 4.5 eV), which is suitable for capacitor's insulating barrier, for sparking plug's insulating. Also, aluminum oxide is utilized in insulation for furnaces or other protection in thermal operation, chemical catalyst tanks (Samant & Dahotre 2009, p. 970). Physical properties of alumina and silicon ceramics are listed in Table 1.

Table 1. Ceramics properties (Sola et al. 2010, p. 5414, Tangwarodomnukun, Wang, Huang & Zhu 2012, p. 39, Li, Chen, Guo, Tao et al. 2017, p.371, Lee & Cheng 2015 p. 402, Garcia-Giron, et al. 2016, p. 549, Chen, Hsiao, Wang et al. 2015, p. 1725, Hanon, Akman, Oztoprak,Gunes et al. 2012, p. 915, Bharatish, Narasimha Murthy, Anand et al. 2013, p. 23, Yan, Li, Sezer et al. 2011, p. 2806).

Name of ceramics	Alumina (Al_2O_3)	Silicon (Si)
Electrical insulation [Ω*cm]	$10^{14} \div 10^{15}$	
Mechanical strength [MPa]	300 ÷ 630	
Compressive strength [GPa]	2 ÷ 4	
Hardness [GPa]	15 ÷ 19	
Vickers hardness [HV]	1300-1700	
Thermal conductivity [W/(m*K)]	20 ÷ 40	130
Density [g/cm^3]	3.75 ÷ 3.97	2.3

Table 1. Ceramics properties (Sola et al. 2010, p. 5414, Tangwarodomnukun, Wang, Huang & Zhu 2012, p. 39, Li, Chen, Guo, Tao et al. 2017, p.371, Lee & Cheng 2015 p. 402, Garcia-Giron, et al. 2016, p. 549, Chen, Hsiao, Wang et al. 2015, p. 1725, Hanon, Akman, Oztoprak,Gunes et al. 2012, p. 915, Bharatish, Narasimha Murthy, Anand et al. 2013, p. 23, Yan, Li, Sezer et al. 2011, p. 2806).

Thermal diffusivity [m^2/s]	$7.58* 10^{-6}$	$8*10^{-5}$
Melting temperature [K]	2327	1687
Dissociation temperature [K]	3250	
Vaporization temperature [K]	3776	
Diffuse reflectance (1064 nm)	0.84	
Optical absorption α (1064 nm) [cm^{-1}]	10.90	
Absorbtion length α^{-1} [cm]	0.09	
Specific heat capacity (at 298 K) [J/(kg*K)]	775-880	

Nonetheless, ceramics can be easily damaged due to high inherent brittleness. Consequently, these obstacles set limitation on ceramics processing. At this point, traditional machining methods are substituted by precise laser processing. Contactless of the process excludes tool ware, vibrations and hindering forces. High removal efficiency, low power demands and medium capital investments make laser machining profitable. (Samant & Dahotre 2009, p. 973-974, Wang et al. 2017, p. 1157)

Ceramics usually are laborious and time-consuming to machine with conventional methods, due to brittleness. Often the final result does not fit in tolerances and has crucial defects. In contrast, laser processing as a non-contact method allows more careful machining, eliminates tool wear and surface damage, and expands complex geometry opportunities. (Yang et al. 2012, p. 3643, Mishra & Yadava 2015, p. 89) Also, laser machining is comparatively inexpensive, controllable and suitable for ceramics processing operations (Hanon et al. 2012, p. 913). Highly intense beam of light hits the workpiece surface, the energy is absorbed and converted into heat. The HAZ (heat affected zone) melts in the center and vaporizes if temperature of vaporization was attained. Thermal changes also happen at the edges of HAZ, but material is not modifying considerably because of decreasing of heat input density toward sides. Although, HAZ commonly can be seen with the naked eye. The ablation means local material removing by vaporization or other effects, which are investigated further.

Although lasers require professional staff and careful maintenance. For instance, optics inside laser setup must be well protected and cleaned on a regular basis. Otherwise dust on optics consumes energy and burns. The whole construction should be accurately aligned and preserved from external vibrations. In case of misalignment the output energy density strongly differs from one, which declared by the manufacturer. It happens due to defocusing of laser beam or simply by setting the workpiece not in the right distance from output window. When shielding gas, for example, nitrogen is utilized the distance between workpiece and nozzle must be also kept appropriately (Samant & Dahotre 2009, p. 983, Adelmann & Hellmann 2015, p.81). Sometimes there are too much debris during laser machining that nozzle became clogged. Basically, all abovementioned means that laser processing might be a powerful tool for processing ceramics, but it needs to be perfectly adjusted and applied properly.

2 INFORMATION ABOUT LASER ABLATION OF CERAMIC MATERIALS

This chapter observes current publications regarding laser ablation of ceramics. The commonly used laser types for ceramics are highlighted. Parameters, which characterize processing quality are mentioned. However, the chapter mainly focus on liquid-assisted laser processing and its advantages over air surrounding laser machining.

In addition, reviewed several studies of cavitation bubble, shock wave and plasma formation. The general laser parameters which responsible for crater quality are defined. Also, the ablation mechanism is explained in detail.

1.1 Preferred lasers

Pulsed Nd:YAG, CO_2, excimer (KrF), and vanadate laser are suitable for ceramics ablation (Samant & Dahotre 2009, p. 973, p. 983). CO2 laser usually have continuous wave (cw) regime, which is applied for macro-processing, or for drilling thin alumina plates (Samant & Dahotre 2009, p. 981), while pulsed lasers allow well-controllable parameters, providing effective monitoring and regulation over procedure. Therefore, researchers give preference to pulse regimes regardless of wavelength. (Ramoli et al. 2017, p. 113) On ceramics the clearer correlations between removal rate and energy density are made in pulse regime. Also, pulses contribute to decrease of recast layer and micro-cracks. (Samant & Dahotre 2009, p. 978) Additionally, the ablated depth is in a direct ratio with peak power, pulse duration and number of pulses (Hanon et al. 2012, p. 913).

1.2 Laser processing quality

The main quality characteristics of drilled hole are circularity, taper, HAZ and cracks, so the following laser processing parameters should be adjusted to obtain better hole quality: laser energy density, pulse width, frequency of pulses and focal plane position (f.p.p). (Wang et al. 2017, p. 1157)

As a rule, specifically CO_2 laser is utilized for ceramic processing. The CO_2 laser wavelength (10,6 μm) has high absorption rate for ceramics, particularly for alumina and aluminum nitride ceramics (Lee & Cheng 2015, p. 400). However, CO_2 laser sets usually have high power (around 3 kW) and are equipped with two dimensions transmission gear and shielding gas nozzle, what makes them useful for cutting operations (Lee & Cheng 2015, p. 415). But, for precise drilling of ceramics Nd:YAG lasers are used. In spite of good precision and effective control of process parameters, the method of pulse impinging has defects such as taper and splashes of recast material around crater. The pulse frequency affects hole taper angle. The taper angle represents contrast between inlet and outlet diameters. (Samant & Dahotre 2009, p. 983)

To overcome the second hindrance (spatters) several approaches are widely implemented. First to mention there are different liquid-assisted laser machining methods (Charee, Tangwarodomnukun & Dumkum 2016, p. 209). The most common, simple, and affordable technique is an applying of water layer onto the treated surface. Depending on a processed material, a certain liquid viscosity and refractive index are required, so water can be changed to some ethyl contained solutions (Garcia-Giron et al. 2016, p. 548). Also, the liquid may cover the workpiece completely (Fig 1) or not (the plate is submerged in liquid but only up to the top), has different layer's depths, the workpiece can be soaked through or only moisturized on the surface, or liquid may come to working area by droplets through nozzle directly to ablated zone. In addition, preheating reduces spatter, and implementation of specific nozzles' configurations prevents redeposition. The next subheading shows a method of laser ablation in presence of liquid in details.

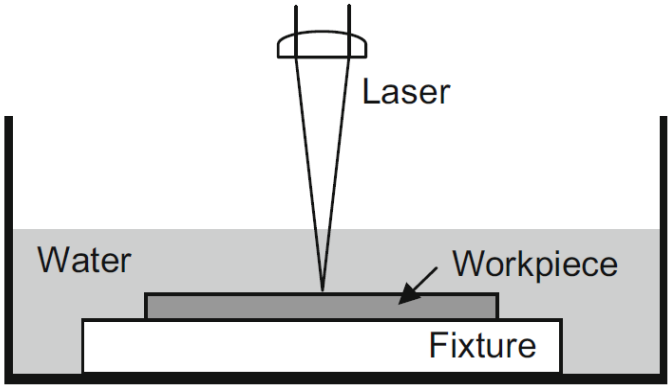

Figure 1. The most common setup for underwater laser processing (Charee, Tangwarodomnukun & Dumkum 2014, p. 21).

1.3 Liquid-assisted laser ablation

Ablation in the presence of liquid (mostly water) was experimentally investigated in a number of researches. Because of improved efficiency and better quality comparing with air ablation, liquid-assisted method gives benefits to variety of application (drilling, cutting, etching, surface cleaning, peening, milling) (Wee, Ng, Prathama & Zheng 2011, p. 62, Tangwarodomnukun 2012, p. 39, Wang et.al. 2018, p.5636). In addition to improved quality the method is inexpensive in installation and maintenance. (Wang et al. 2017, p. 1159)

Water usage contributes to riddance from ablated material's debris and moderate cooling of workpiece. Various research works were concentrated on comparison of ablation in air and liquid surrounding space (Silvennoinen, Kaakkunen, Paivasaari & Vahimaa 2012, p. 865, Li et al. 2009, 78, Lopez, Bakrania, Coupland & Marimuthu 2016, p. 2689, Wee et al. 2011, p. 62). Unfortunately, case of thick layer of liquid above surface leads to such problems as breakdown, formation of cavitation bubble and beam propagation impairment (bending, self-focusing, energy absorption). For ultrashort pulses machining the recommended layer is several microns in order to minimize unwanted effects. However, liquid makes ablation more efficient comparing with ablation in air. For instance, experiment with thin layer of distilled sprayed water on silicon plate's surface interacted by IR laser beam (femtosecond pulses with fluence up to 26,0 J/cm2) showed the advantage of water-assisted ablation. The surface and hole were clean, without resolidified particles, which meant that post-cleaning process was not needed (Fig. 2). Also, the ablation speed was two times higher than for ablation in air (Fig. 3). The positive effects can be explained by obvious lack of debris near the top, which ensures free laser beam path thought. Therefore, water spray assistance (Fig. 4) noticeably enhances the result. (Silvennoinen et al. 2012, p. 866)

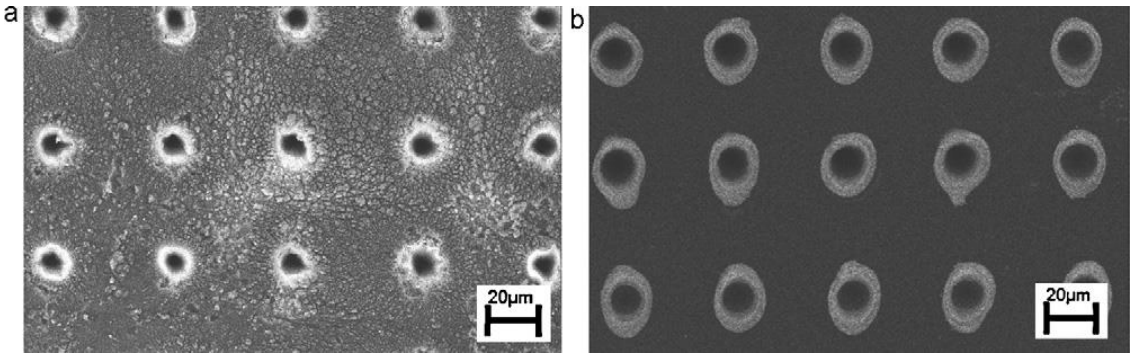

Figure 2. Images of the laser ablation results without water spray (a) and with water spray assistance (b) (Silvennoinen et al. 2012, p. 867).

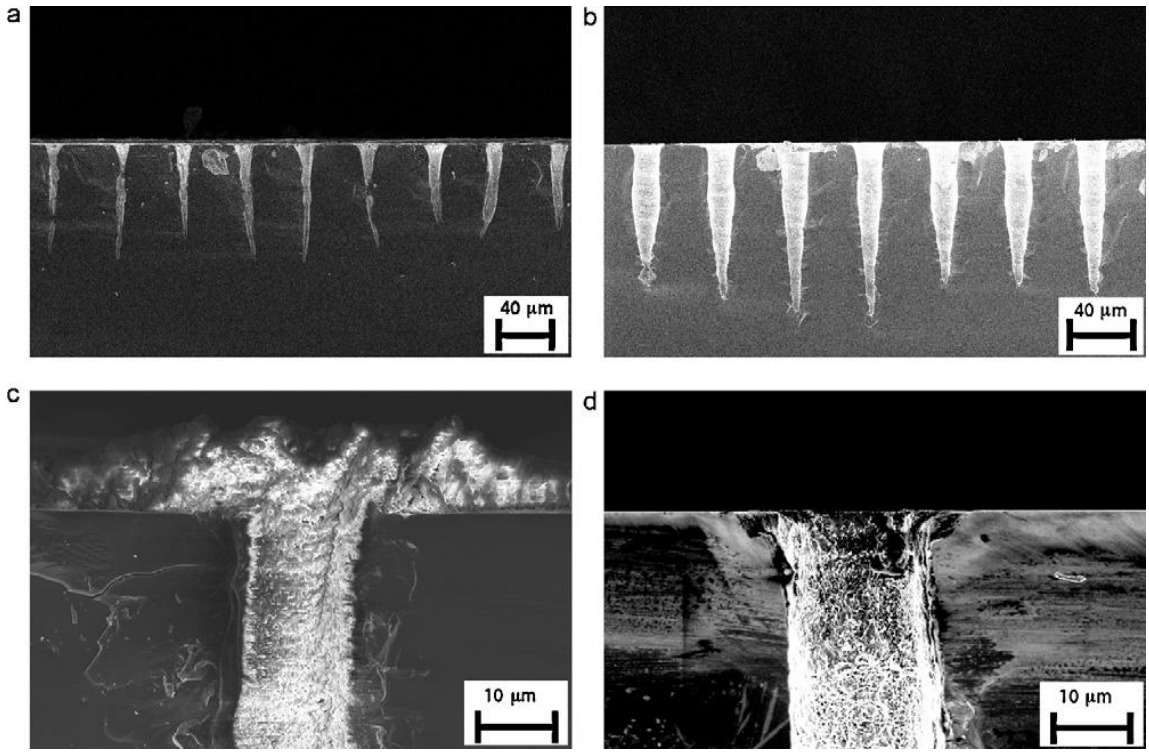

Figure 3. Cross sectional SEM-images of hole made in silicon plate without water spray (a, c) and with water spray assistance (b, d) (Silvennoinen et al. 2012, p. 867).

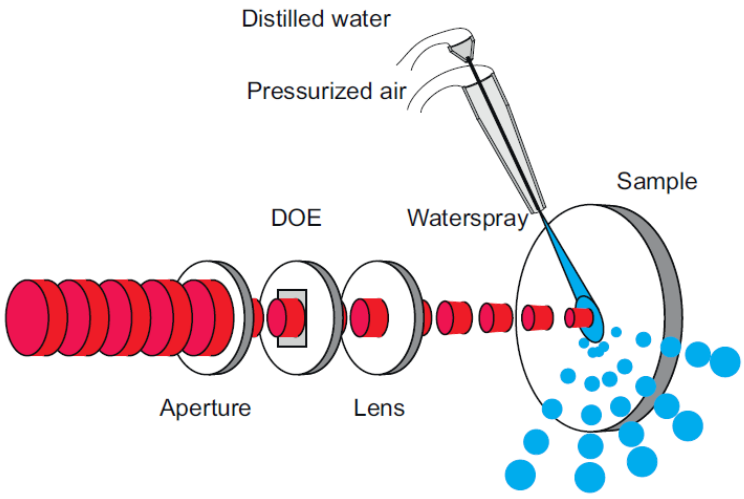

Figure 4. Scheme of water spray assisted laser ablation setup (Silvennoinen et al. 2012, p.866).

Similarly, reducing of both debris and HAZ was noticed via ablation in water in comparison with air ablation in experiment with silicon plate and 355 nm of laser wavelength. But the

bubbles in water film occurred at high frequencies scattered the laser beam. (Xu, Hu & Lei 2014, p. 670)

Underwater ns PLA was conducted on silicon carbide wafer with Nd:YAG laser (1.064 μm wavelength). The optimal water layer thickness was found out to be about 1 mm. Less debris, cracks, and HAZ were observed while mentioned water layer thickness was applied. (Iwatani, Doan & Fushinobu 2012, p. 520)

Performing an underwater CO_2 laser machining of alumina substrate confirmed advantages of water-assistance. Quality improvement, less cracks and heat damage due to water cooling effect were noticed. A high recoil pressure of water helped to throw away molten parts and avoid its re-solidification near entrance. The optimal water layer thickness was established to be a 3-4 mm. (Yan et al. 2011, p. 2806)

Increasing in depth of a hole was also noticed during alcohol-assisted laser drilling of silicon carbide wafer. While processing in air condition the crater quality suffered from debris. But not only appearance was spoiled. Redeposited debris scattered the incident light, what resulted in absorption of laser energy by them. After some time, the amount of debris became sufficient to prevent a hole from increasing in depth. Machining of SiC wafer of 250 μm in thickness was performed with Ti:sapphire laser. The wavelength was 800 nm, power density was 3.1 GW/cm^2. On the top surface one alcohol droplet had been put before laser irradiation. By volatilization of alcohol carrying away ablated material was realized. The circular holes of 40 μm in diameter were made. On photographs the obvious advantages of alcohol assisting are clearly seen (Fig. 5). Debris did not surround hole's entrance. Moreover, post cleaning with the same liquid easily helped to obtain excellent surface look. Also, alcohol did not lead to additional thermal damage. (Li et al. 2009, 79)

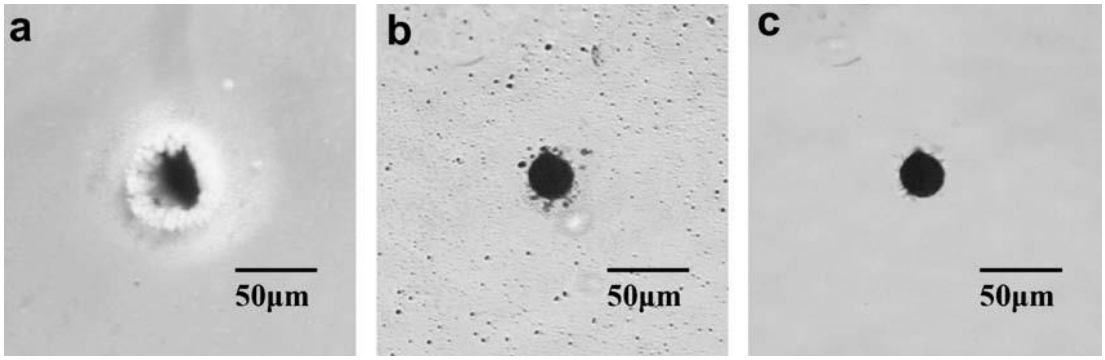

Figure 5. Micro-photos of drilled holes on top of SiC wafer by femtosecond laser (a) experiment in air, (b) experiment with alcohol, (c) experiment with alcohol-assisted laser drilling and following alcohol washing (Li et al. 2009, p.80).

The benefit of alcohol assistance was noticed while laser drilling of silicon carbide wafer with 355 nm wavelength (Fig. 6). Methanol provided better quality in comparison with air and water laser drilling. In particular, the cleaning effect and smoother surface due to minimized particle deposition were obtained. Also, the layer thickness had an influence on the result. The solvent has lower boiling point, so cooling made smaller HAZ. (Wee, Khoong, Tan & Lim 2011, p. 1275)

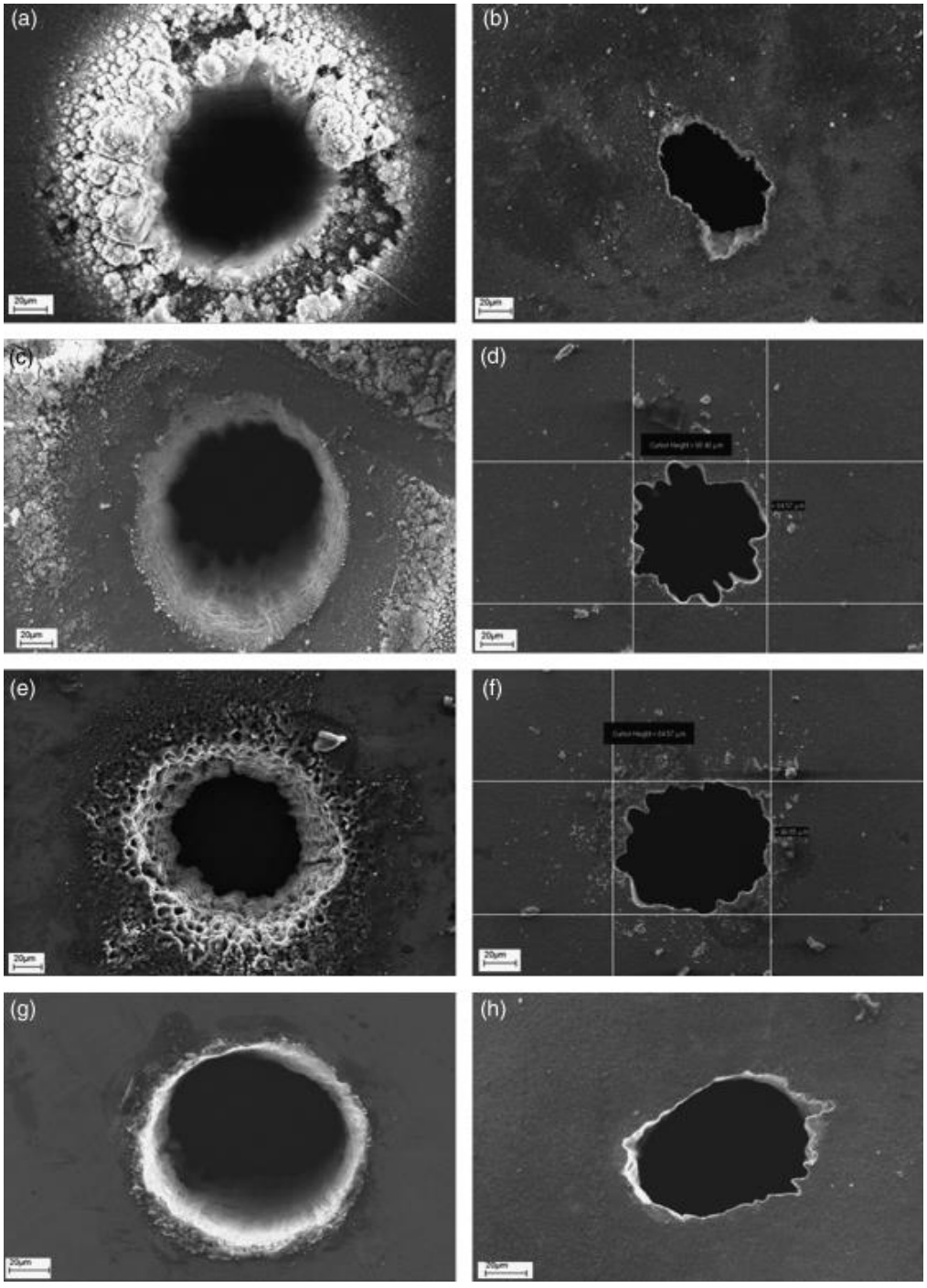

Figure 6. Images of drilled holes in SiC wafer under different surroundings. The left column shows entrance holes, the right column shows exit holes. Air surroundings a-b, stagnant water c-d, water stream e-f, methanol g-h. (Wee et al. 2011, p. 1266).

Caustic potash (KOH) solution also was used in Al_2O_3 laser machining. Cleaning and reducing of defects was pointed out. (Genfu, Wei & Xuehui 2012, p. 2479)

Droplet assisted laser micromachining (DAML) was a modernization of a dry pulse laser ablation (PLA) (Fig. 7). DAML experiments were carried out on tungsten carbide (WC) plate with thickness of 10 mm irradiated by nanosecond Nd:YAG laser (355 nm, 8ns pulse duration) (Lopez et al. 2016, p. 2690). In PLA material vaporized only partly, the bigger part solidified as melt on crater walls. Ejected particles mostly deposited around hole as a dross. (Lopez et al. 2016, p. 2689)

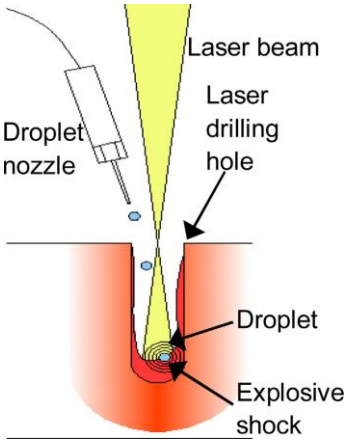

Figure 7. Sketch of droplet assisted laser micromachining (Lopez et al. 2016, p. 2690).

Through the nozzle a droplet of controlled volume, 150 μm in size were applied synchronically with laser frequency of 10 Hz (Lopez et al. 2016, p. 2690).

The advantage of the DAML technique is based on impulse shock pressure, which is realized by explosive vaporization of droplet trapped in irradiated zone. The improvements of DAML comparing to PLA are following: material removal rate was increased by 75%, minimization of spatter by 71% and decrease of taper angle. Cross sectional surface profiles were taken to reveal an explicit contrast between spoiled PLA crater's edges and smooth DAML walls free from redeposited material (Fig. 8). Moreover, the actual depth was two times deeper in DAML ablation, while diameters for both methods were roughly equal. The utilizing DAML was recommended for metal, alloys and ceramics. (Lopez et al. 2016, p. 2694)

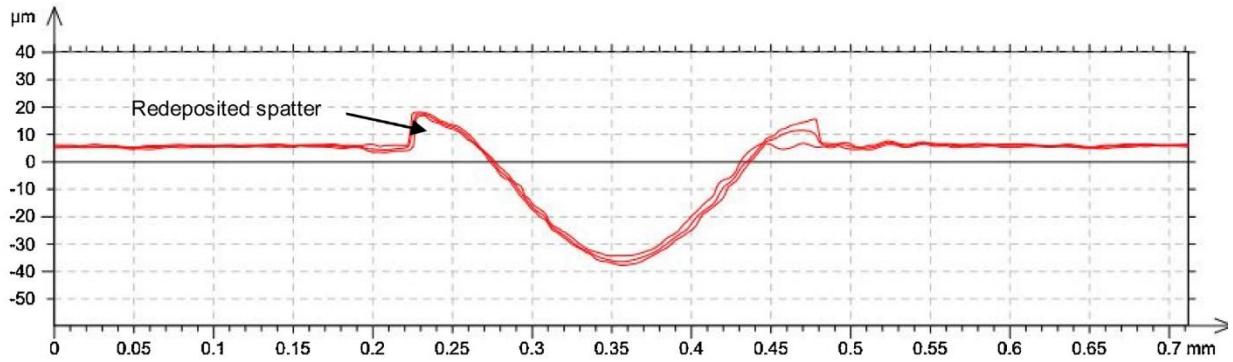

Cross sectional surface profile of PLA process

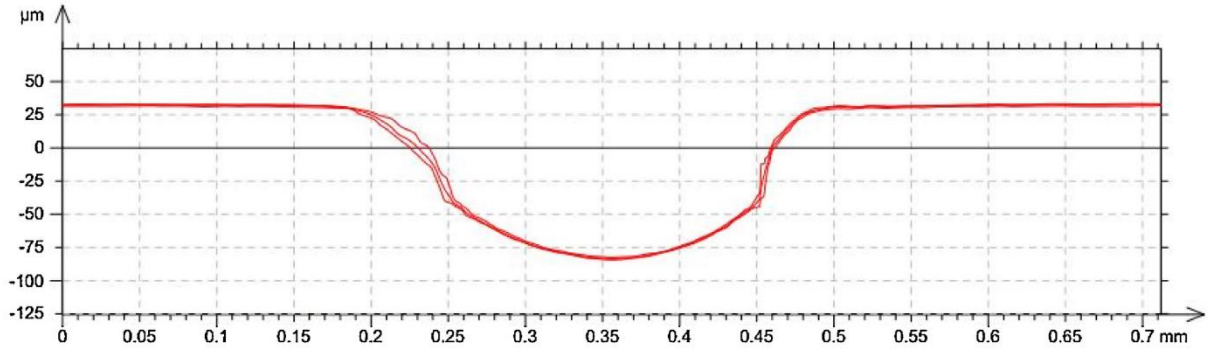

Cross sectional surface profile of DALM process

Figure 8. Cross sectional surface profiles of PLA and DAML process after ablation under the same laser parameters (Lopez et al. 2016, p. 2691).

Experiment with alumina ceramic ablated in liquid surrounding layer with nanosecond laser pulses (Nd:YAG laser, 1064 nm, 11 W) confirmed the same beneficial contribution of liquid. First trials in water showed that ablation yield raised by 26 times in water surrounding in comparison with air. That was explained by cavitation bubbles, which hastened the ablation. Second trial in ethylene glycol surrounding provided negative result of liquid assistance. The high viscosity and density inhibited shock wave and following cavitation bubble. (Garcia-Giron et al. 2016, p. 553)

In addition, the water layer thickness should be selected appropriately. The Figure 9 presents experimental ablated depth in alumina ceramic along with varied water thicknesses and focal plan position (f.p.p.). (Garcia-Giron et al. 2016, p. 551) Out from three layers thicknesses 3, 5 and 10 mm the best one for alumina was 5 mm. As seen from the experiments, positioning f.p.p. below surface results in deeper ablation. Also, to achieve effective ablation result an optimal layer thickness must be taken. Initially, the depth increases with layer increases but only up to some value, after surpassing it, the ablation yield declines. (Garcia-Giron et al. 2016, p. 553)

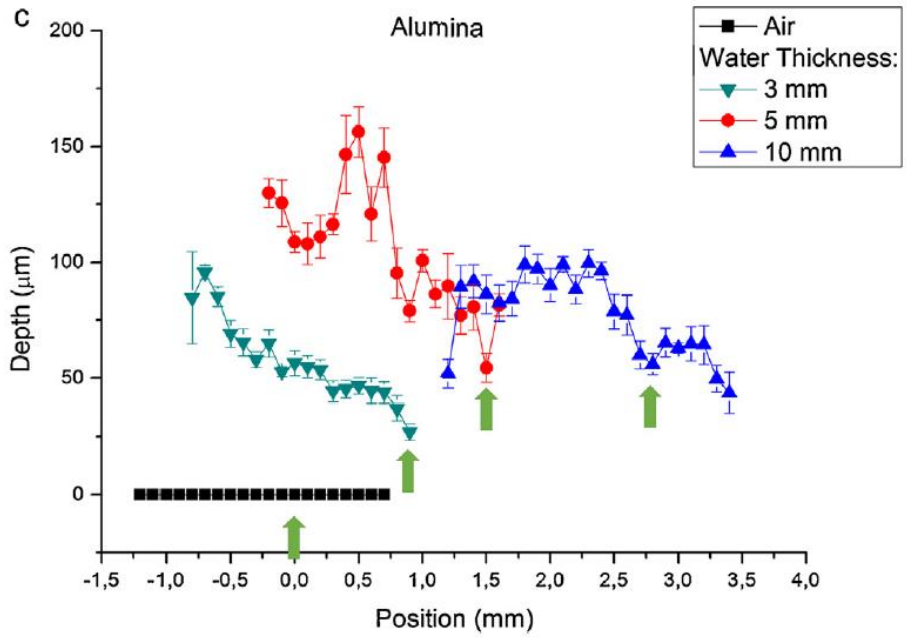

Figure 9. Dependence ablated depth in alumina from f.p.p. regarding three water layers thicknesses 3, 5 and 10 mm (Garcia-Giron et al. 2016, p. 551).

The water layer can be stagnant or flowing. The second case provides approximately constant layer thickness (Fig. 10). It makes experiment reliable and accurate for estimations. Furthermore, the whole layer is never vaporized, regardless of a power of cw regime. The steam of water remove debris from surface helping to clean. (Charee et al. 2016, p. 210, Wee et al. 2011, p. 64)

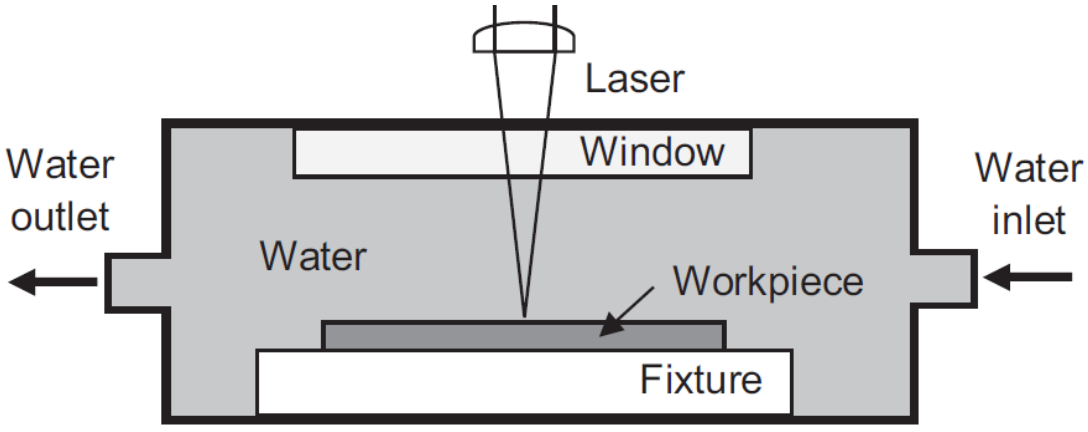

Figure 10. Underwater laser ablation with flow stream (Charee et al. 2016, p. 210).

Hole drilling experiments were conducted in air and under a stream of water in order to understand the modified laser ablation. Silicon wafers of 200 µm in thickness were interacted by 355nm-laser under 1 mm thick water layer. The hole (diameter was 50 µm) was drilled by

repeatable circular motion of laser beam with size of 25 μm. In experiment on same parameters but in air surrounding the hole covered 40 μm2, due to great bulk accumulation on the sides of a wall. Thus, the exit rim did have extremely poor circularity. In spite of water refraction of laser radiation, the water-assisted drilling achieved much better exit hole circularity. (Wee et al. 2011, p. 63-64)

The work (Wee et al. 2011, p. 62) was mainly devoted to quality analysis relatively specific laser parameters and selecting the best ones. For example, the low frequency and high peak power were suggested to reduce spatter. But the taper angle is smoother by higher frequencies and by lower power densities. In addition, influence of f.p.p. on quality was studied. Shifting focal point inside plate resulted in limiting of exposed to spatter area and taper angle decreasing. (Wee et al. 2011, p. 68) Unfortunately, information about Rayleigh length was not provided. Nevertheless, it could be appropriately long for used plate because of noticeable improvement of through hole circularity and debris amount decrease. The importance of long Rayleigh length becomes apparent during drilling. Since the depth of hole increases, the beam has to pass this depth to affect material, but energy density no longer enough to surpass the ablation threshold. With longer Rayleigh length energy density sustain closer to maximum along with distance, allowing to overcome ablation level. (Adelmann & Hellmann 2015, p. 83)

In conclusion, the experimental research (Wee et al. 2011, p.70) demonstrates surface cleaning effect, acceleration of ablation rate, widening of holes diameters and contraction of taper angle by water-assisted laser machining as compared to conventional laser ablation. Nonetheless, severe surface deterioration by bubbles impaired quality (see paragraph 1.4). In addition, it is difficult to retain a constant water layer thickness at in underwater laser ablation, but in case of water stream it is not a problem.

To acquire better cooling effect from liquid usage, flowing stream can be replaced by water-jet. The technique is rather profitable. Original construction is supplemented with a water pipe with the nozzle at the end of path, which is directed toward a workpiece. The idea is that the laser beam goes inside this water jet like in optical fiber, totally reflecting from jet column's walls. In other words, it prolongates initial laser focal length.

More sophisticated facilitation for laser cutting setup is waterjet hybrid machine. This apparatus is aimed for factory usage and mass production, due to higher efficiency (high removal rate). Waterjet cools workpiece and reduce thermal damage from laser energy input. Basically, the

high-pressure waterjet removes not a molten material but softened material (below melting temperature). So, the process requires lower heat input. Scheme of this apparatus is presented on the Figure 11, the waterjet nozzle had been placed by side under varied angles, while the laser beam (1080 nm wavelength) was directed perpendicularly to workpiece. (Tangwarodomnukun et al. 2012, p. 40)

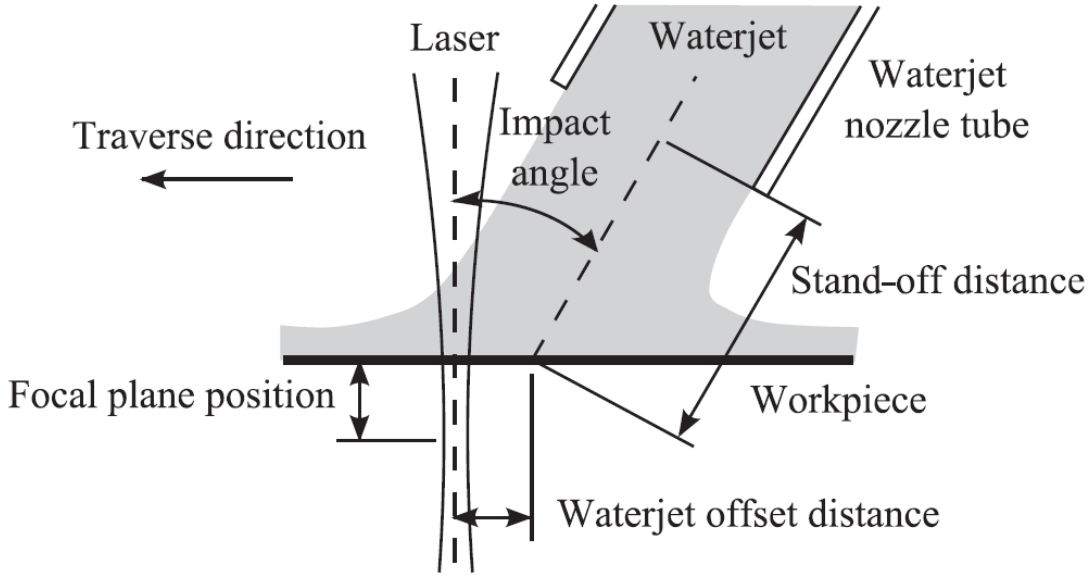

Figure 11. Sketch of hybrid laser-waterjet apparatus (Tangwarodomnukun et al. 2012, p. 41).

Experiments were made on silicone sheet with the thickness of 700 μm. Waterjet parameters such as pressure (5, 10, 15 and 20 MPa, distance 0.4 mm and angle (30, 40, 50 and 60 degrees) were adjusted to influence on the process. In addition to high removal rate waterjet minimized recast layer and produced almost damage-free cut. In simple terms, the waterjet works similar to shielding gas. (Tangwarodomnukun et al. 2012, p. 41)

The same result of waterjet was noticed in Lu et al. 2014: improved surface and inside hole quality, smaller amount of recast slag. Waterjet was released from a 0.7 mm diameter nozzle with speed up to 28 m/s. The Al_2O_3 plate was drilled with Nd:YAG laser (maximum average power 500 W, wavelength 1.064 μm, frequency up to 100 Hz, pulse length 0.1-10 ms). In addition, the enhanced removal rate was observed. (Lu & Genfu 2014, p. 22)

Other techniques can also ensure profit from laser ablation in water environment. Silicon wafer 508 μm in thickness was treated by laser irradiation with following parameters: wavelength 1064 nm, average laser power 30 W, frequency 30-250 kHz, pulse duration 120 ns. During ablation process 5 mm layer of water was influenced by ultrasound. The experiment showed

similar features as in research works mentioned above. Debris and molten material were flushed away, water cooled down the silicon wafer. High frequency ultrasonic waves were a powerful tool for cutting deep and clean grooves. Also, the work highlighted superiority of flowing water stream above the ordinary underwater assembly. (Charee et al. 2016, p. 215)

Other work on ultrasound assisting in water confined environment revealed similar benefits. But in that case ultrasound machine was submerged in water, not attached to the backing of workpiece. The higher ablation yield with cleaning (less debris deposition) and cooling were provided by bubbles explosion and increased pressure. (Liu, Gao, Wu et al. 2014, p. 90)

In conclusion, main advantages of liquid assistance are cooling, narrowing of HAZ and debris removing (Charee et al. 2016, p. 210, Wee et al. 2011, p. 62, Wang et al. 2017, p. 1168).

1.4 Cavitation bubble

This subchapter analyzes and clarifies the effect of bubbles formation and explosive boiling during liquid-assisted laser treatment.

The main point is prevailing advantages of water use. Reduction of laser energy in water in general along with scattering stirring movements and reflection does not result in low ablation rate. However, water vaporization causes the wall sides porosity. Superheating of water in small volume by high power laser density leads to bubbles nucleation which leads to explosive boiling. If water is heated above the liquid-vapor critical point (T_c 647 K) and pressure is (218 atm), it becomes supercritical fluid with dramatically altered properties. But even in vicinity of T_c bubbles formation is triggered. So, the part of layer above ablated spot is superheated and saturation parameters are almost reached. Subsequently, expansion of bubbles nucleation guarantees pushing of ablated material away. When explosive boiling happens a huge amount of material is forced to eject. (Wee et al. 2011, p. 69)

The picture 12 indicates spherical hollows as locations of bubbles nucleation. Probably, their explosion strongly contributed to material emission. (Wee et al. 2011, p. 64)

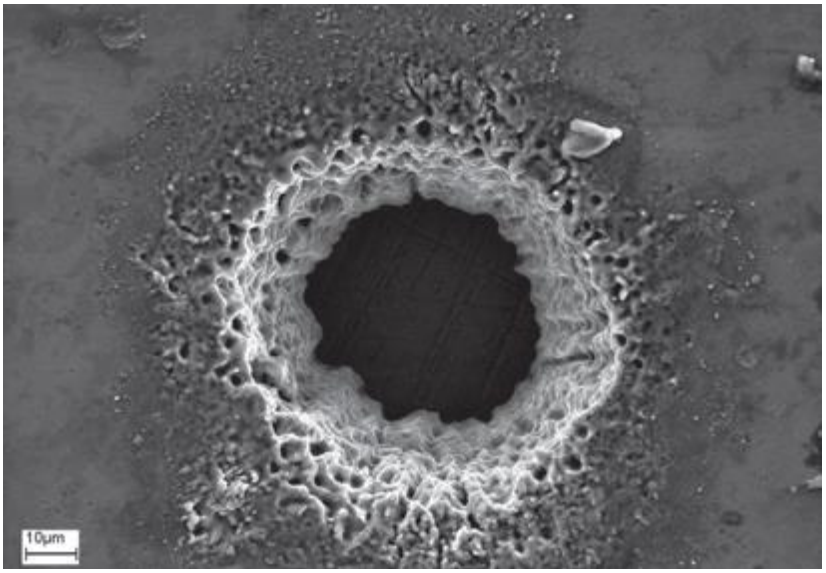

Figure 12. Morphology on top surface of silicon plate after laser ablation with assistance of Flowing water film (Wee et al. 2011, p. 64).

Collapsing of cavitation bubble or bubbles boosts debris ejection via released pressure. This shock pressure can damage workpiece by causing cracks. (Charee et al. 2016, p. 219)

Cavitation bubble and shock wave were observed in experiment of laser ablation under 5 mm layer of distilled water. An epoxy resin plate was irradiated with 1,064 nm laser wavelength. The shock wave was triggered by collapse of cavitation bubble. In addition, trials with extra absorbent coating pointed out higher energy of bubble and increased shock wave speed (increased shock pressure) due to more laser energy was absorbed. The underwater laser shock process (LSP) was conditioned by plasma vapors. (Nguyen et al. 2013, p. 1109) The Figure 13 shows dynamics of cavitation bubble after the end of laser irradiation. On the first image shock and stress waves are seen with emerging hemispherical cavitation bubble. The cavitation bubble expanded for 230 µs up to 4 mm in diameter, then gradually shrank and collapsed. (Nguyen et al. 2013, p. 1113)

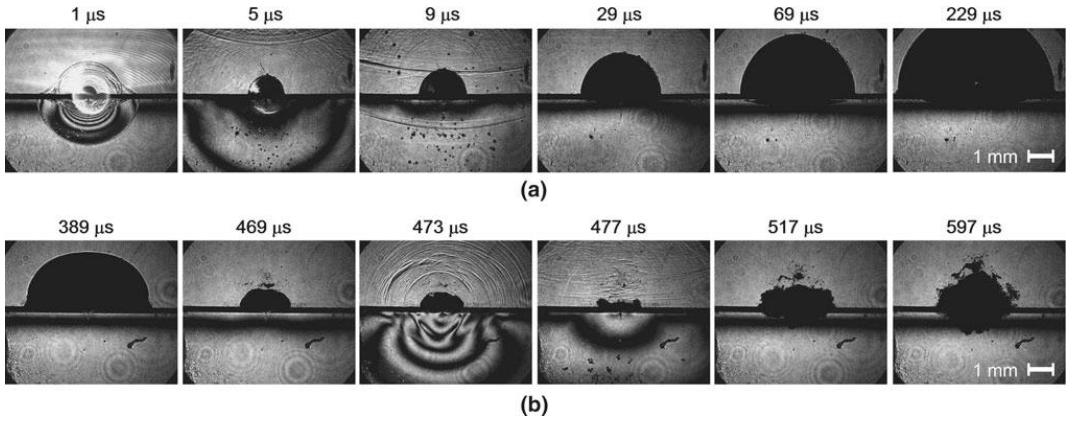

Figure 13. Cavitation bubble and shock wave during underwater laser ablation of epoxy resin (Nguyen et al. 2013, p. 1114).

Pulsed laser ablation in liquid (PLAL) is widely studied. When laser beam strikes surface, excessive energy transforms into shock wave, causing disturbances. The shock wave goes in all directions, into liquid and inwards the workpiece. (Yan & Chrisey 2012, p. 207) PLAL generates bubbles near the surface line, and this effect has two explanations. Firstly, it is an explosive boiling mechanism due to overheating of liquid. Secondly, the cavitation bubble formation because of changes in pressure, not in temperature. But they can be integrated in laser-induced bubble formation. (Yan & Chrisey 2012, p. 209)

In conclusion, when material submerged in liquid undergoes laser irradiation, two interactions occur: laser-liquid and laser-material. If laser density is high, the optical breakdown and plasma formation complement the interaction. Plasma starts to expand producing shock wave. After shock wave the cavitation bubble starts to expand and collapse. (Garcia-Giron et al. 2016, p. 548)

1.5 Parameters responsible for a high quality of surface

This part examines some parameters, which also affect the ablation result but were overlooked or scarcely mentioned on previous sections.

Inert gases flow is beneficial mean to flush away debris. Besides, gas protects material from oxidation and works as a cooling mechanism.

The focus position is significantly important in drilling. Usually the best results are carried out by focusing on surface. But it is applicable only for thin plates in consideration of Rayleigh

length. In case of thick plates, the focal point is better to be shifted inward the workpiece at a reasonable distance. The long Rayleigh length provides small and immutable beam size for longer distances, consequently the optimum power density is achieved. Due to smaller wavelength of Nd:YAG lasers in comparison with CO_2 laser, the beam is focused to narrower diameter and Rayleigh length becomes longer.

To visualize relationship between beam characteristics there are following formulas presented (Sola et al. 2010, p. 5416).

$$D_{bw} = \frac{4fM^2\lambda}{\pi D_0}$$ (Equation 1)

Diameter at focal point (D_{bw}) is the narrowest width of beam. It is determined by focal length (f), beam quality factor M^2, wavelength (λ) and diameter of beam before lenses (D_0). Power density reaches the maximum number at focal point.

$$R = \frac{\pi D_{bw}^2}{4M^2\lambda}$$ (Equation 2)

where R is the Rayleigh length, and it depends on focal diameter.

Dependency on f.p.p. was observed with experiments on Al_2O_3 ceramic substrate and 11 W Nd:YAG laser. The alumina plate 0.5 mm in thickness was irradiated by a laser beam with 1064 nm wavelength, at focal point, below and above. The result is shown in the Figure 1.14, where it can be seen that proper machining can be made only in vicinity of focal point. Ablated volume at optimal position was 188 μm3 per one 8 ns pulse (Sola et al. 2010, p. 5414).

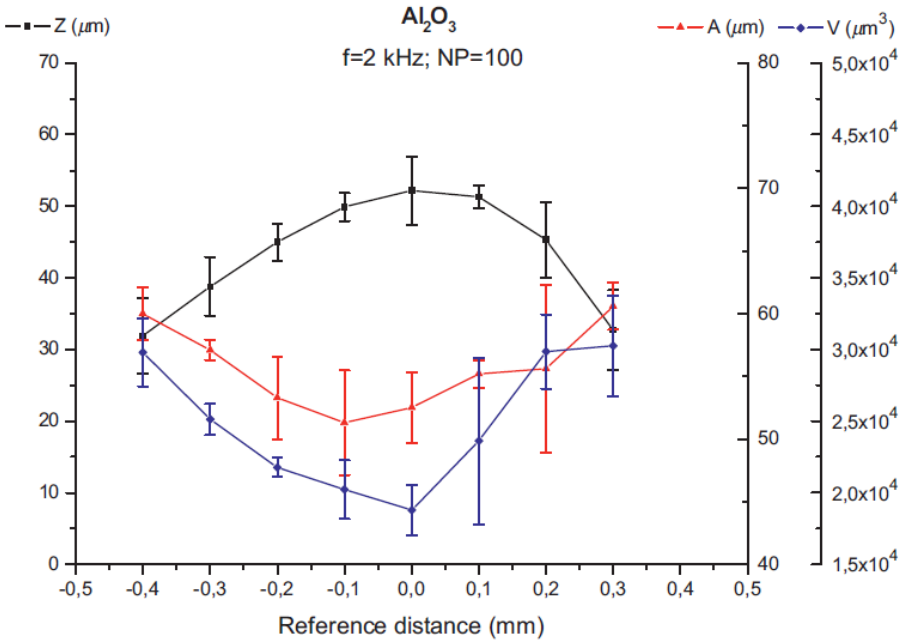

Figure 14. Geometrical parameters of ablation alumina ceramic with 2.45 mJ energy impulse, where Z is depth, A is width, and V is a volume of an ablated material (Sola et al. 2010, p. 5416).

The other work (Adelmann & Hellmann 2015) confirms abovementioned results (Sola et al. 2010) of important role of f.p.p. Al_2O_3 and AlN ceramics served as specimens for laser drilling trials with varied f.p.p. The obvious correlation between entrance hole and f.p.p. was noticed: the closer to focal, the narrower hole diameter. Nevertheless, bottom hole diameter depended on plate thickness. For instance, on thick samples (up to 1.5 mm) shifting f.p.p. inside (on negative distance) resulted in narrow bottom hole diameter. (Adelmann & Hellmann 2015, p. 83)

Additionally, it is well-known that angle of incidence influences absorption. Brewster's angle implies no reflection, therefore the alignment of workpiece to be near the Brewster's angle improves absorption and efficiency significantly. For ceramics Brewster's angle is approximately 80 degrees. (Ramoli et al. 2017, p. 114)

Pulsed lasers working in IR region allows energy transforms into heat, the heat penetrates material according to its conductivity. Furthermore, this heat results in required processing time, removal depth, defects and other parameters. (Ramoli et al. 2017, p. 114)

Enhancement of ablation rate can also be explained via plasma pressure. The point is that water restricts plasma in volume, therefore makes plasma pressure higher. Consequently, the ablated

materials are thrown away. Apart of the benefits, plasma also may causes shielding effect, preventing laser beam to reach surface (Lopez et al. 2016, p. 2690).

Raising the issue of holes circularity, there are several main parameters to mention, which affect it. The entrance hole became more circular with higher laser power. But that correlation is working while hole diameter grows up to some certain value. Whereas the exit hole is more circular for both higher power and larger hole diameter cases. Taper is smoother with higher power. The HAZ is influenced by pulse laser frequency: higher frequencies reduce HAZ during experiments with constant laser power. The confirmatory drilling experiments were made on alumina ceramics 2 mm in thickness with CO_2 laser. (Bharatish et al. 2013, p. 32)

Other experiment confirmed that entrance hole diameter is not in direct proportionality with pulse duration and pick power due to significant material re-solidification on the entrance (Kacar et al. 2009, p. 2014).

It was noted by a number of authors that different types of laser beam polarization show different drilling efficiency (Cristoforetti et.al. 2010, p.219, Kraus et.al. 2010, p.22305, Allegre et.al. 2012, p.1). For example, steels are predisposed to obtain equal diameter and depth of drilled holed under a doughnut-shaped beam with azimuthal polarization. (Meier, Romano & Feuer, 2007, p.329).

1.6 Ablation process in details

Basically, when laser beam hits surface there occurs three main phenomena: reflection, transmission and absorption. Only absorption is in charge of workpiece modification via laser-matter interaction and consequent heating of the material. Spectral absorptivity describes the percentage ratio of energy of definite wavelength, which was absorbed. But, in case of deep drilling the beam is reflected from walls multiple times. That increases a number of surfaces to absorb energy. (Samant et al. 2009, p. 974)

This absorbed energy transforms into heat. Energy conversion obeys to conduction, convection and surface radiation effects. Fourier's second law interprets heat transfer by following equation (Samant et al. 2009, p. 975):

$$\frac{\partial \mathrm{T(x,y,z,t)}}{\partial \mathrm{t}} = \alpha(\mathrm{T}) \left[\frac{\partial^2 \mathrm{T(x,y,z,t)}}{\partial^2 \mathrm{x}} + \frac{\partial^2 \mathrm{T(x,y,z,t)}}{\partial^2 \mathrm{y}} + \frac{\partial^2 \mathrm{T(x,y,z,t)}}{\partial^2 \mathrm{z}} \right] \text{(Equation 3)}$$

where T depicts the temperature distribution at the bulk sample,

x, y, z are the Cartesian coordinates,

t is current time during heating,

a is the thermal diffusivity coefficient.

Thermal diffusivity is determined by temperature (heat) conductivity, thermal conductivity and density, and also depends on temperature since each of its components is substantially undergoes changes with temperature fluctuation. The relationship of them is listed below (Samant et al. 2009, p. 975):

$$\alpha(\mathrm{T}) = \frac{\mathrm{k}\,(\mathrm{T})}{\rho(\mathrm{T})\mathrm{c}(\mathrm{T})}$$ (Equation 4)

Here k is a temperature (heat) conductivity, ρ is a material density, and c is heat capacity.

In that way, transformed heat warms up workpiece making it melt and vaporize afterwards (Fig. 15).

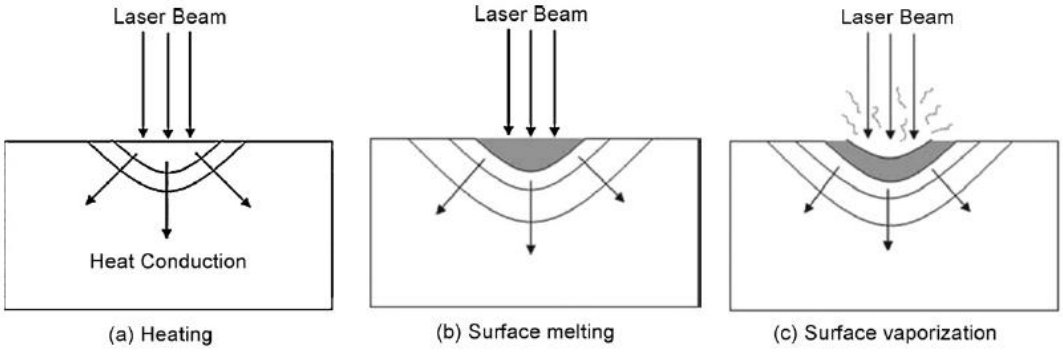

Figure 15. Sketch of laser-surface interactions: heating, melting, vaporization (Samant et al. 2009, p. 975).

After reaching and passing the ablation threshold removing of material obeys to the Beer-Lambert law, and removed volume is in direct logarithmic dependence from laser density (Mishra & Yadava 2015, p. 92).

Generally speaking, an ablation process is not fully investigated regarding involved mechanisms. Composition and material properties intensely affect ablation behavior. Also, during heating chemical and thermal properties generally are changed, making estimation of

ablation process complicated. Wavelength, optical beam properties, and pulse characteristics are important for absorbtion. (Sola et al. 2011, p. 5413)

It is logical, that ablation rate grows with laser power density (Fig. 16). Contrariwise, larger interaction time does not result in better ablation rate, but makes it decline (Fig. 17). That can be explained by prolongated distance to upper surface of workpiece. If the f.p.p. is placed on zero position, after some time of interaction the power density is not high enough for material physical transformation. Thus, longer ablation time makes upper surface go down, decreasing power density on it and reducing ablation rate. (Tong, Bai, Zhank & Ye 2013, p. 6815)

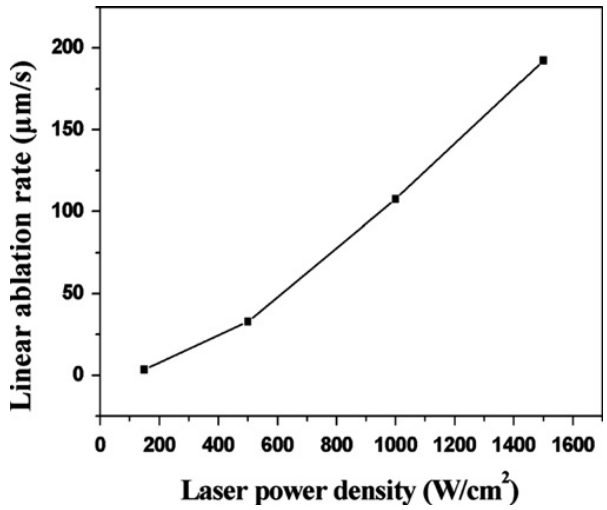

Figure 16. Relationship between ablation rate and laser power density (Tong et al. 2013, p. 6815).

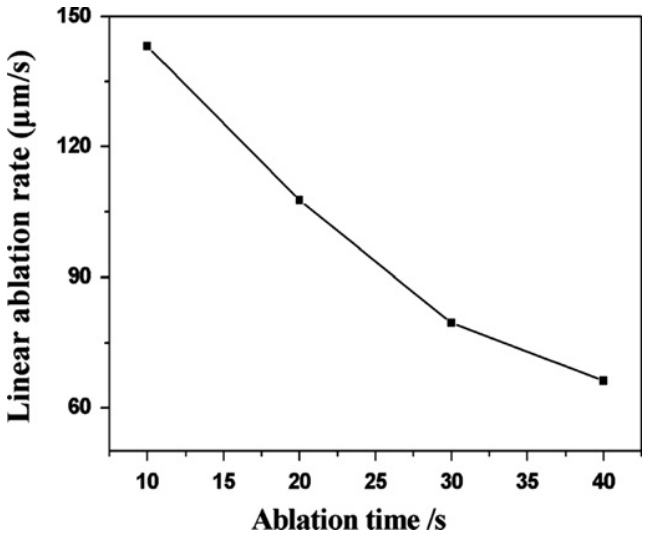

Figure 17. Relationship between ablation rate and time of laser interaction (power density 1000 W/cm^2) (Tong et al. 2013, p. 6818).

In an experimental study C/SiC composite was ablated by Nd:YAG pulsed laser with wavelength 1064 nm and power density up to 1500 W/cm^2. The center of HAZ was severely heated up to approximately 3500 ℃, providing decomposition and sublimation of material. Such high temperature made burning gas mixture above the spot, where beam strikes the surface. Near transitional zone of HAZ no melting occurred, the gases from central part can escape there and re-nucleate. In spite of lower temperature of transition zone, it was still sufficiently high for SiO_2 volatilization. (Tong et al. 2013, p. 6816)

In case of extremely high temperature, the ablation process skips melting stage. Sublimation of overheated surface provides explosive boiling, which removes material. (Ramoli et al. 2017, p. 113)

It was proposed that three concentric ablation regions exist regarding dominating processes. In central zone blast and sublimations occur, which are great mechanisms for material extrusion. In transitional zone ablation is mainly performed via vaporization. On the third zone, only oxidation and other thermal-induced processes occur. (Liu, Zhang, Jiang et al. 2011, p. 4303)

1.7 Modeling of laser ablation process

Many factors including abovementioned affect laser ablation process. While the thermal effects are simpler to define and describe, the chemical effects are more complicated and demand significantly more sophisticated and expensive methods of research. Removal mechanism of IR waves carries out due to heat transfer. Since the present work devoted to laser irradiation in near-and far-IR region, thermal effects prevail over photo-chemical ones, which mostly relate to UV lasers. So, modeling of ablation process is focused on thermal aspects. (Ramoli et al. 2017, p. 113)

Laser energy becomes absorbed by the workpiece and transform into energy of heat. This heat is conducted inward the plate according to thermal equation, and also a convection from bottom surface to backing or surrounding air occurs. As a result, the temperature distribution field is organized through the workpiece. Thermal equations can be one-, two- and three-dimensional calculations, based on desired accuracy and workpiece geometry. The temperature distribution corresponds to process parameters and material characteristics, eventually forecasting required

time to perform machining, removed depth, and HAZ. (Yang et al. 2012, p. 3645, Samant & Dahotre 2010, p. 1)

Thermal distribution has the most important role in analyzing and understanding the nature of ablation. It depends on the workpiece thermophysical characteristic such as thermal conductivity, critical phase temperatures, density, heat capacity, thermal diffusivity. Moreover, thermal distribution is influenced by workpiece geometry like thickness, length, width. In addition, heat input, output heat flow, surface area, boundary conditions and initial temperature should be taken into consideration. All these parameters are responsible for melting, sublimation, vaporization and ultimate ablation with other possible thermal and chemical processes (for example, dissociation). Knowing temperature distribution provides possibility for predicting laser machining result and selecting suitable laser parameters. (Yang et al. 2012, p. 3645; Samant & Dahotre 2009, p. 976)

One problem is varying numerical value of material characteristics during laser-material interaction. It means dependency thermal conductivity, heat capacity, thermal diffusivity, density from constantly changing temperature. Firstly, hindrance of definition the exact value of physical characteristic, which relates to a small temperature region. Secondly, adjustment of formulas for integrated values and their dependency. Lastly, for combined materials it is an obstacle to define physic characteristics, because it is not a primitive summation of components, but a definitely new material with nonidentical characteristics. For instance, composite materials prone to greatly change their chemical and thermal properties during laser irradiation (Tong et al. 2013, p. 6818).

In case of high power density, the material vaporizes and ionizes, causing plasma formation. The temperature of plasma is approximately 50,000 degrees. That provides the near-surface effect of plasma shielding (Fig. 18). Plasma occurs above irradiated spot in a shape of plume, reduces input laser energy, and it mentioned in a number of works (sometimes the gas nozzle is installed to blow away plasma plume). In simple terms, after laser optical breakdown the formed plasma cloud absorbs light completely (Mishra & Yadava, p. 92). However, up to now this effect is not well estimated in research studies. Also, it is difficult to detect plasma formation during ablation because the degree of ionization should be calculated. (Samant & Dahotre 2009, p. 977) Thus, in present work plasma absorption and reflection of laser energy is neglected.

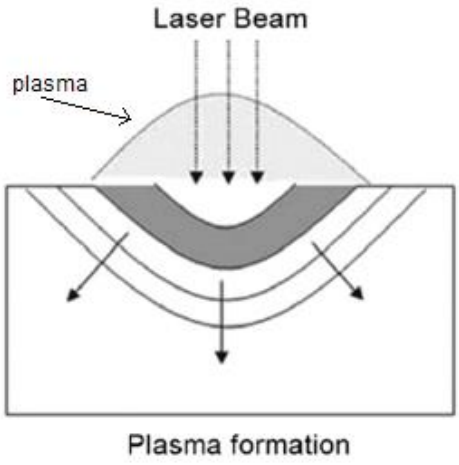

Figure 18. Sketch of plasma formation (Samant & Dahotre 2009, p. 975).

The way of reducing initial amount of heat input in estimation is justifiable by these unresolved effects. In that way, the initial energy is an energy of heating workpiece, but not the energy of laser beam. The most appropriate way to draw an ablation model, is a considering laser beam as an ordinal, but dimensionally limited, heat source, which is placed on the upper workpiece surface. So, the light energy is transformed into thermal energy.

After heating melting process takes place. But the melting process requires at least a threshold power density. For ceramics approximate power density of 10^5 W/cm^2 provides obtaining the melting temperature by surface of workpiece. The figure 19 shows change of temperature during laser action and after laser stops. The t_p on figure 19 means time of irradiation. By that time the surface reaches maximum temperature. The graph basically represents either continuous laser irradiation or heating during one pulse of pulsed regime and cooling before next pulse. (Samant & Dahotre 2009, p. 976)

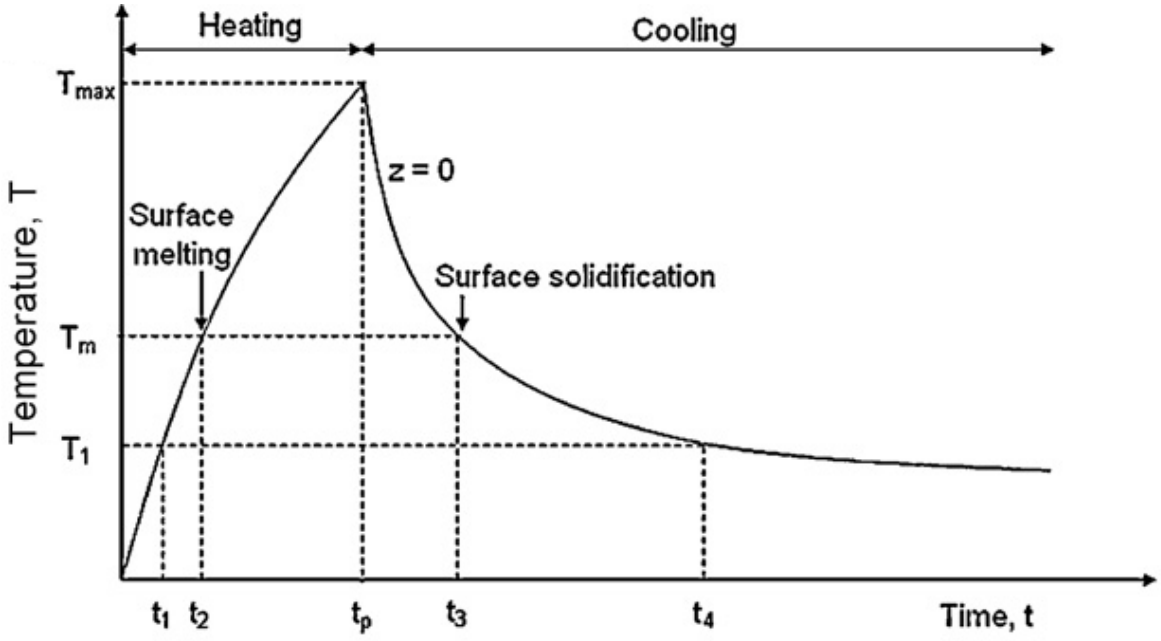

Figure 19. Graph of surface temperature dependence by time (Samant & Dahotre 2009, p. 976).

When temperature passes beyond the boiling point, the vaporization process removes material away. At that time the liquid-vapor boundary goes deeper and ablation via vaporization occurs. The velocity of movement of liquid-vapor boundary is in direct ratio with absorbed energy. But it is in inverse proportion with density, boiling point temperature and latent heat of vaporization. The relationship is presented in the following equation (Samant & Dahotre 2009, p. 977):

$$V = \frac{Q_a}{\rho(cT_b + L_v)} \quad \text{(Equation 5)}$$

Table 2. Meanings of symbols in equation 5

V	Velocity of liquid-vapor boundary
Q_a	Absorbed laser energy
P	Density of workpiece
C	Heat capacity of workpiece
T_b	Boiling temperature
L_v	Latent heat of vaporization

Incorporation of all thermal processes before ablation threshold is surpassed, ablation

itself and cooling mechanism together makes a model of ablation process. The model shows required time for making cavity of predefined depth.

According to alumina critical temperatures, it is possible to heat it up to 2327 K in solid state, and heat the liquid alumina up to 3250 K. After that alumina dissociate to aluminum vapor and atomic oxygen consuming energy (Equation 6). The liquid phase explodes because of recoil pressure. This recoil pressure significantly contributes to removing process. (Samant & Dahotre 2009, p. 982)

$Al_2O_3 = 2Al(l) + \frac{3}{2}O_2(g)$ (Equation 6)

Not only removal rate but melt flow and heat transfer are influenced by recoil pressure. Recoil pressure depends on the surface temperature, and in case of high temperature the removal is made by recoil force instead of evaporation. (Yang, Chen & Zhang 2016, p. 141) In that case the input laser energy is consumed by kinetic energy of vapors, latent heat of vaporization and by heat conductivity of liquid phase. (Yang et al, 2016, p. 144) So, the increase of laser energy input leads to strengthening of vapor recoil pressure, due to the latent heat of vaporization and the heat conductivity of liquid phase are constant. (Yang et al. 2016, p. 148) The Figure 20 presents scheme monocrystalline silicon ablation with the recoil pressure depicted as arrows (Xu et al. 2014, p. 668).

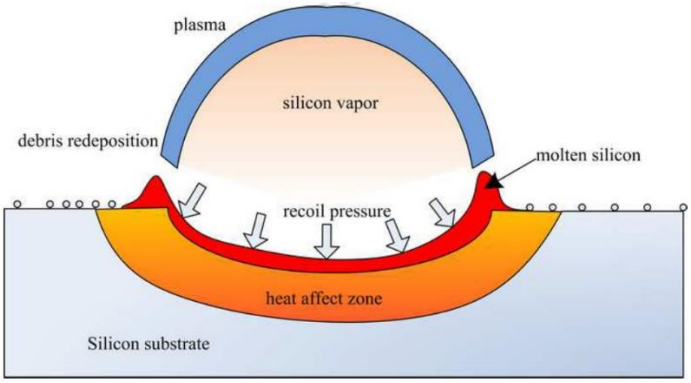

Figure 20. Sketch of air laser ablation of monocrystalline silicon with nanosecond pulses in 355 nm wavelength (Xu et al. 2014, p. 668).

3 EXPERIMENTAL RESULTS

This chapter deals with description of utilized hardware, conduction of experiments and emphasizes results of water-assisted laser ablation of ceramics.

2.1 Experimental setup

Mainly the work is devoted to study an interaction of laser radiation and ceramic materials. Consequently, several laser sets were used during experimental research. Pulsed and continuous regimes were used, near-infrared and infrared laser irradiation were applied to the workpieces.

The principal goal was achieving spherical structure above ablated region.

1) Ytterbium fiber laser system Laser center «Mini Marker 2» at ITMO University laboratory

- Wavelength 1.07 μm
- Maximum power 20 W
- Beam radius 25 μm.
- Power density up to 10 GW/m^2
- Pulse duration 200 ns
- Frequency 20 kHz

Figure 21. System of surface laser modification Mini-Marker 2.

2) Ytterbium fiber cw-laser IPG Photonics LK-100-W at ITMO University laboratory

- Wavelength 1.07 μm
- Maximum power 100 W (109 W in reality)
- Beam radius about 30 μm
- Power density up to 40 GW/m^2

Figure 22. Ytterbium fiber single-mode laser LK-100-W.

3) Ytterbium fiber pulsed laser IPG Photonics YLPN 50 W at ITMO University laboratory

- Wavelength 1.07 μm
- Maximum power 50 W
- Beam radius about 50 μm
- Power density up to 6 GW/m^2
- Pulse duration 140 ns
- Frequency 50-100 kHz

Figure 23. Ytterbium fiber single-mode laser YLPN 50 W.

4) CO_2 TRUMPF TLF2700 HQ laser at LUT Laser laboratory

Figure 24. CO_2 laser source.

Figure 25. Control board of CO_2 laser.

Figure 26. Barometer of shielding gas pressure.

Figure 27. CO_2 laser workplace, protecting housing.

- Wavelength 10.6 μm
- Maximum power 2.7 kW
- Beam radius 64 μm
- Power density up to 210 GW/m^2
- Rayleigh length 0.894 mm
- Beam quality K>0.85
- Focal length 2.5 mm
- Shielding pressure (nitrogen) 2 bars
- Frequency 99900 Hz

2.2 Experimental procedure

Experimental setup was based on utilizing laser source. Laser beam went through lens and focused on the surface of workpiece. Beam diameter varied from 50 µm to 130 µm depending on the used laser set. Sample was drenched with liquid (usually water). Irradiation of YAG lasers have high transmittance through water (Samant & Dahotre 2009, p. 977). A droplet was applied on the top and mashed. Between laser shooting moisturizing procedure repeated, because of rapid vaporization, and mainly because of laser heated the workpiece. To film the process a high-speed camera was used. Pictures allowed to watch the ablation and sphere formation processes in detail and in slow motion. Special light source was installed to illuminate workpiece's surface in order to be seen via camera. The process installation is pictured on the Figure 28 in basic details.

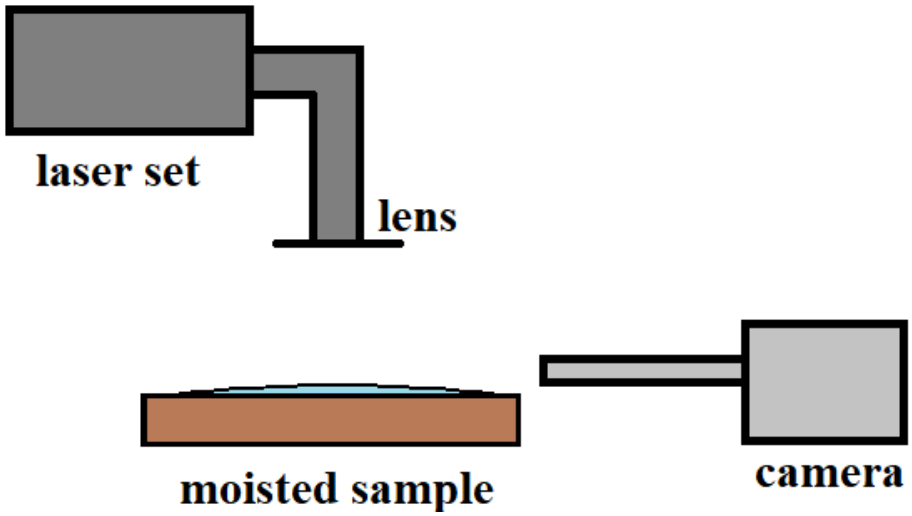

Figure 28. Scheme of experimental setup.

In some cases, protection shield, glass to collect debris, cuvette with water, UV filter were used to facilitate analyses. Caliper were used to measure thickness of plates and their dimensions. Other instrumentations are mentioned in following subsections in order of their purpose.

2.3 Experimental materials and results of near IR laser oblation

Primary experiments were performed on ordinal constructional ceramic tiles made from alumina. One side of tiles was covered with enamel, but in most cases the irradiated side was a rear side and enamel did not interrupt the input laser energy flow. In the number of cases the

laser action produced a formation of a glassy thin-walled sphere above the hole, which as to author's knowledge has not been mentioned in previous researches.

The following experimental tests included usage of other ceramics samples to see their reaction. Finally, nine different ceramic materials undergo 100W cw-laser irradiation. All samples were moisted with water on the upper side each time before the laser had shot.

The chemical composition, material characteristics and laser-material interactions are listed below.

1) Firstly, the initial sample of alumina-silicate ceramics, which chemical composition was detected by Energy-dispersive X-ray spectroscopy (EDX) analysis (see Chapter 2.11 for EDX studying).

Table 3. Chemical composition of alumina-silicate ceramics (sample #1)

SiO_2	72%
Al_2O_3	27%
FeO	1%

Thickness of plate was 7 mm. After one second of laser exposure glass sphere formed above crater.

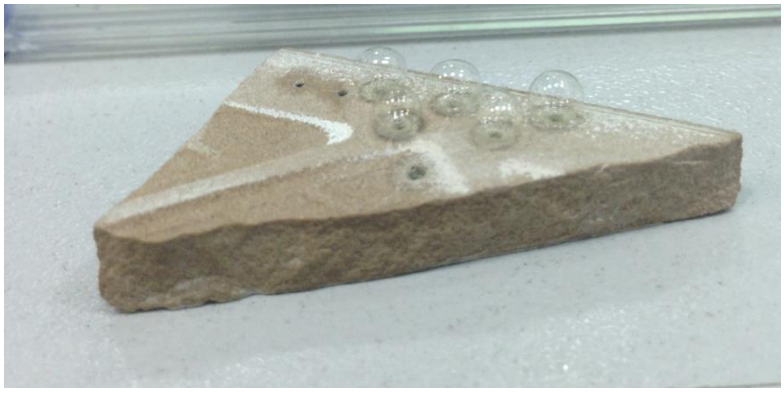

Figure 29. Plate of alumina-silicate ceramics with produced spheres above craters. Continuous-wave mode, power density 40 GW/m^2, time of laser impact 1 second.

2) Ceramics plate baked of green clay.

Table 4. Chemical composition of alumina-silicate ceramics (sample #2)

Si_2O_3	47.8%
Al_2O_3	15.9%
CaO	12.1%
Fe_2O_3	4.0%
K_2O	2.83%
MgO	1.73%
TiO_2	0.65%
Na_2O	0.26%
MnO	0.04%

Experiments with 100 W cw ytterbium laser also showed spheres appearance. From 40% to 75% of power (41.3 to 82.1 W) and 3-5 seconds of exposure spheres were obtained, their diameters were about 1-3 mm. In addition, it is important to note that melt around and inside crater had black color, while obtained glass spheres had more gray tint and loose transparency in comparison with spheres on other materials.

Figure 30. Plate of silicon dioxide ceramics with produced spheres above craters. Continuous-wave mode, power density 40 GW/m^2, time of laser impact 1 second.

3) Ceramics plate baked of Italian clay with decorative chippings.

Table 5. Chemical composition of alumina-silicate ceramics (sample #3).

Si_2O_3	48.92%
Al_2O_3	24.88%

Table 5. Chemical composition of alumina-silicate ceramics (sample #3).

Fe_2O_3	12.28%
K_2O	3.20%
MgO	0.93%
TiO_2	0.85%
CaO	0.28%
Na_2O	0.19%

Decorative chippings, which inserted throughout all ceramic body, contributed to intense flying and splashing of ablation debris. Besides, small (1 mm) spheres were produced only by cw ytterbium laser at 100W power and they did not occur during pulse laser radiation. Thus, experiments were stopped, due to higher power threshold.

4) Two plates of clay with following composition and two temperatures of roasting (1020°C and 1250°C). The first plate did not provide spheres at all, probably, laser irradiation went through the plate. The second plate produced 1-mm-size sphere above the crater with clear edges (all melt was extruded forming sphere).

Table 6. Chemical composition of alumina-silicate ceramics (samples #4.1 and #4.2)

Si_2O_3	51.80%
Al_2O_3	32.60%
Fe_2O_3	4.61%
TiO_2	1.39%
K_2O	1.00%
CaO	0.49%
MgO	0.44%
Na_2O	0.24%

5) Two porcelain samples: ordinary and not parched. The second sample showed the appearance of spheres above the crater and on the bottom side of the plate. This is related to subtlety of plate and free space left below the sample during a lasing.

Table 7. Chemical composition of alumina-silicate ceramics (samples #5.1 and #5.2)

Si_2O_3	53.53%
Al_2O_3	20.50%

Table 7. Chemical composition of alumina-silicate ceramics (samples #5.1 and #5.2)

CaO	8.58%
K_2O	2.20%
Na2O	1.17%
TiO_2	0.98%
Fe_2O_3	0.67%
MgO	0.30%

6) Light ceramics with fireclay PCB/CHF. Spheres with 3-5 mm diameter were made.

Table 8. Chemical composition of alumina ceramics (samples #6).

Al_2O_3	98%

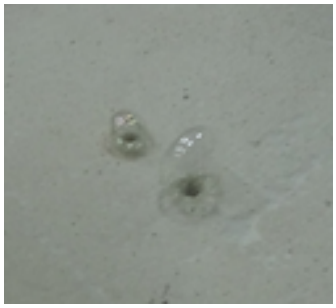

Figure 31. Plate of alumina ceramics with produced spheres above craters. Continuous-wave mode, power 70%, time of laser impact 1 second.

For samples #1, #2 and #5, which are most prone to the formation of spheres, the characteristic values of the final volume, the change in volume after laser off, the time of growth and the rate of inflating were obtained.

Table 9. The averaged results obtained during power P = 50 W, pulse repetition rate f = 100 kHz.

	Sample 1	Sample 2	Sample 5
Time of sphere growth, ms	400	320	132
Final volume of sphere, mm^3	43	170	36
The volume of sphere at end of laser impact, m^3	40	155	28
The rate of inflation, mm^3/s	100	505	230

The spheres obtained on the sample #2 have the largest sizes and the highest rate of their formation. This may indicate a low melt viscosity of the sample and a high absorbency of the liquid, which contributes to the growth of the spheres. While for the sample #5 the time of active growth of the sphere is 2.4 times less, and the final size of the sphere is 4.7 times less than for the sample #2, which may indicate a higher melt viscosity of the composition #5.

2.4 High-speed video monitoring of spheres formation process

High-speed camera AOS X-Motion with the speed of shooting up to 1000 frames/sec was used for observation of the processes of ablation and the formation of the spheres (Fig. 32).

Figure 32. High-speed video camera X-Motion: color, resolution 1280x1024, pixel size 12 μm, shooting speed at full resolution 500 frame per second, speed shooting at reduced resolution 32000 frame per second, dynamic range 10 bit.

Experiment of laser ablation with power density 10 kW/m^2 of sample #1 was recorded by camera and presented in Figure 33. The process of sphere formation from melt after the end of laser exposure took 77 ms. Diameter of sphere was almost 1 mm.

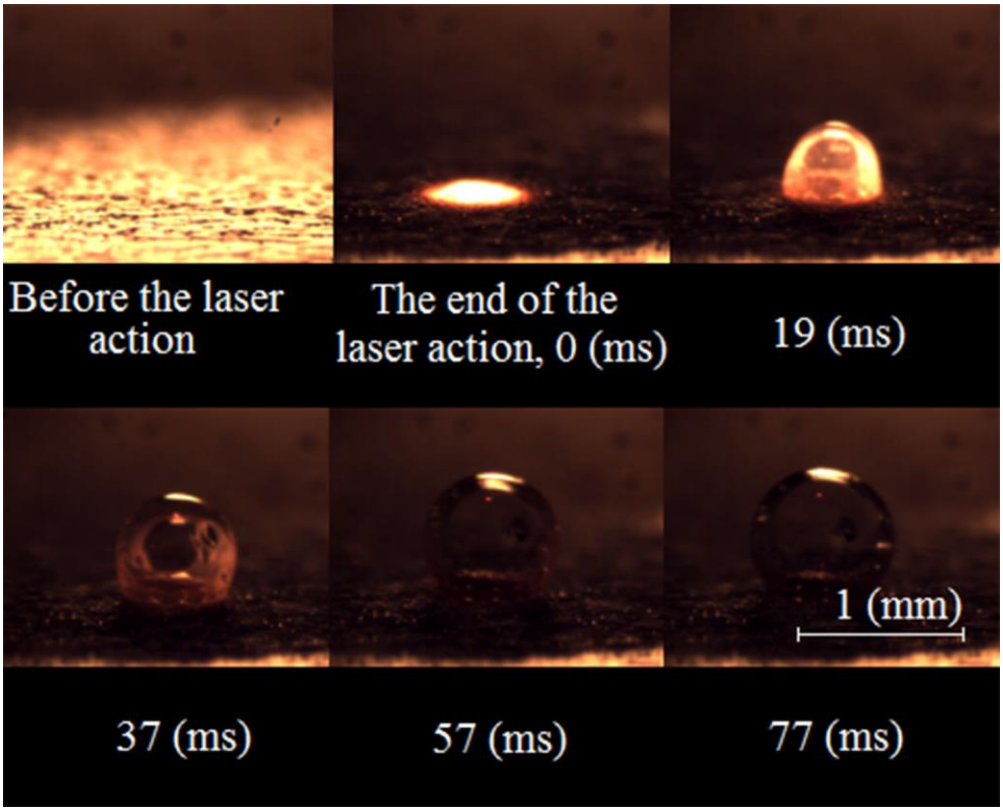

Figure 33. Dynamics of glass sphere formation under pulsed laser exposure with power density 10 kW/m^2 (Sinev, Dobrina, Strusevich, Veiko et al. 2016, p. 546).

Dynamics of sphere parameters (height, width, volume) is shown in Figure 34 after pulsed and continuous laser action. Sphere was being rapidly blown out (speed was approximately 6 mm/s), in the first of 0.1 - 0.3 seconds after the end of laser exposure. The final size of the sphere depends on the power density.

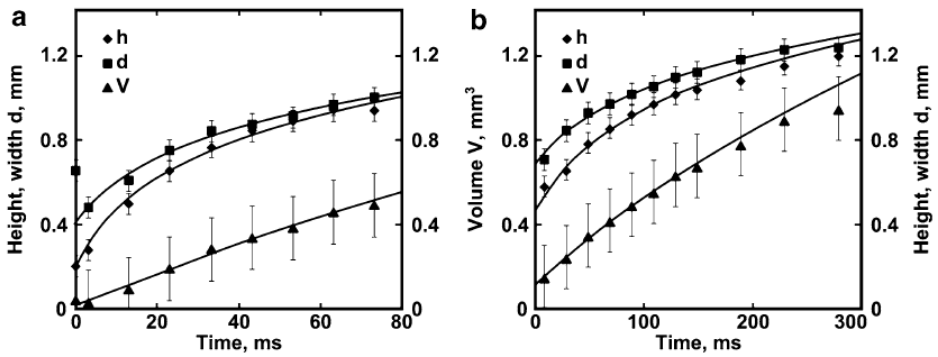

Figure 34. The observed dynamics of spheres geometric parameters: height - h, width – d, V – volume. a) pulsed laser exposure with power density 10 GW/m^2 b) cw-laser exposure with power density 40 GW/m^2. (Sinev et al. 2016, p. 546)

On the first alumina-silicate ceramics spheres of 5 mm in diameter were made when cw-laser was in use, and spheres of 1 mm in diameter were made with impulse laser radiation. These results were accomplished at maximum power density for both laser sets.

In order to study the influence of composition to the result, several new ceramics materials were backed in plate shape. Radiation varied, but the common and essential action is that all plates were drenched with distillate water. So, the initial sample #1 provided sphere formation from melt above crater. The largest spheres 5 mm in diameter were obtained by cw-100W laser (Figure 35).

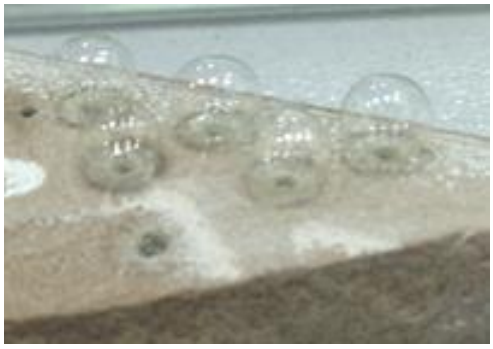

Figure 35. Spheres on sample #1.

The sample #2 also showed an appearance of the spheres with approximate diameter of 5 mm under action of 50 W pulsed laser (Fig. 36). Out of new material (#2-#6) the second sample generated the biggest spheres, due to extended time of vapor pressure.

Figure 36. Spheres on sample #2.

Nevertheless, the sample #5 did not perform as much spheres as previous ones. But the shape of sphere was almost achieved (Fig. 37).

Figure 37. Sphere on sample #5.

The sample #6 usually provided hemispherical melt after 50 W laser radiation exposure (Fig. 38).

Figure 38. Hemisphere on sample #6.

It was found that the most prone to the formation of spheres (spheres are observed in more than 50% of cases) were ceramics with compositions with less aluminum oxide. This may be due to an increase in the temperature thresholds of phase transitions in ceramic materials with an increase in the volume fraction of Al_2O_3 in the composition.

The complete absence of spheres (0% of cases) in case of extra sample, monolithic (non-porous) sample of corundum ceramics was demonstrated. Thus, it was confirmed that the porosity of the material, leading to the ability to absorb water, is a prerequisite for the formation of spheres.

2.6 Kinetics of growth during and after continuous near IR laser impact

The clear expansion of a sphere recorded on the sample # 2 (100W laser, 50 GW/m^2 of power density, 1.5 second of laser on) is presented in Figure 39.

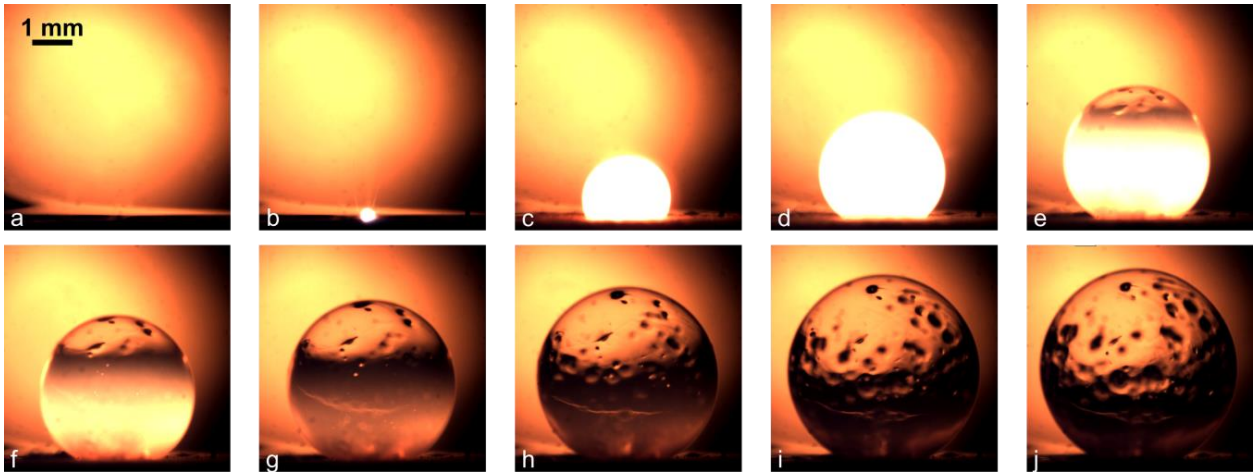

Figure 39. The surface of the ceramic sample
a) before laser treatment;
b) with continuous exposure with a power density of 50 GW/m2;
c) at the end of the exposure (duration 1.5 s);
g-i) 50 ms, 100 ms, 150 ms, 200 ms, 250 ms, 300 ms and 350 ms after laser exposure, respectively.

On the averaged line graph the dynamic during laser irradiation and after it is shown (Fig. 40). The gradual increase in size of melt, which starts right after turning off the laser is obvious (volume began to rise). Under continuous exposure, the melt is influenced by constant vapor pressure, and the kinetics of the melt bath is stable.

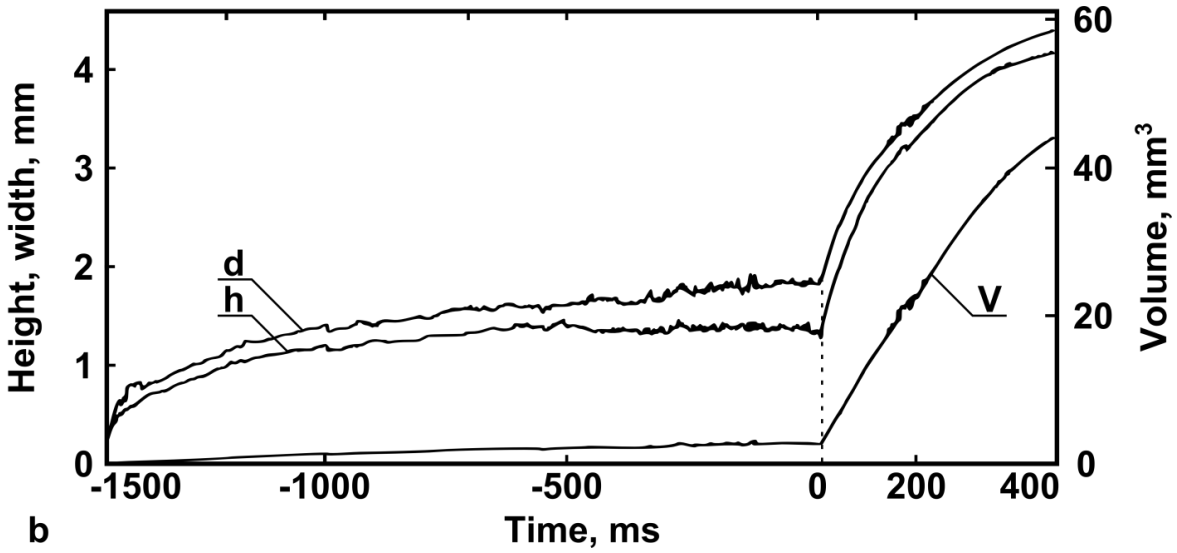

Figure 40. The kinetics of height of the molten bath above the surface of the sample during continuous laser exposure. Zero mark indicates the end of laser exposure.

But kinetics during pulsed laser action significantly differs from kinetics under continuous action. Under the pulsed radiation the height of melt showed significant fluctuations and was unstable throughout the entire time of radiation exposure, reaching ± 0,1 – 0,5 mm. Similar size fluctuations can be related to the vapor pressure of the liquid in the ceramic pores, trying to form a sphere at the end of each pulse. However, the rapid growth of the sphere in both pulsed and continuous exposure occurs after laser exposure. The growth of the sphere occurs during the period of 0.1 - 0.3 s, the threshold value of the pulsed radiation power density required for the formation of spheres was 4 GW / m^2.

Kinetics of growth during and after pulse laser impact is presented on figure 41. The sphere tried to expand between pulses. Unfortunately, the camera records at much lower frequency than pulses, ergo, only discrete frames of these attempts were acquired. Nevertheless, after the end, sphere expansion starts and obeys to the logarithmic law: swiftly grows during first 0.1 seconds and decreases gradually in speed after.

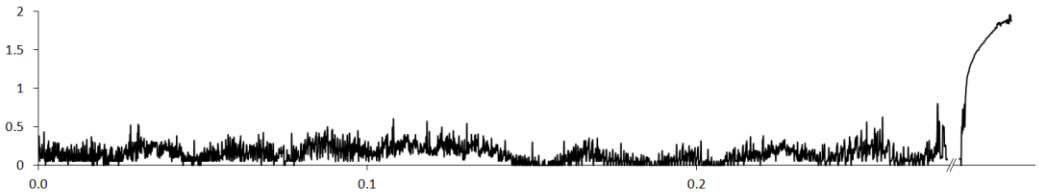

Figure 41. Ytterbium fiber laser ILMI-50, wave length λ = 1070 nm, a power density q ≈ 10 GW/m^2 and pulse duration of τ = 200 ns, the pulse repetition frequency f = 100 kHz.

2.7 Ceramic water-assistant laser ablation with CO_2 laser

This section discusses experiments performed at Lappeenranta University of Technology laboratory "LUT Laser" on the CO_2 TRUMPF TLF2700 HQ laser, the video was recorded by high-speed camera Optronis CR3000x2 (f=55 mm, magnification 0.4x-0.9x) of the same department. For the experiments four ceramics were selected, which have shown the most promising yield of spheres in previous trials at ITMO laboratory. Samples were dipped in water. The first trials were not recorded by camera and results were examined with naked eye.

The sample #1 (SiO_2 72%, Al_2O_3 27%, Fe_2O_3 1%) showed an appearance of glass hemispheres on top side of sample, up to 1.5 mm in diameter, induced by low laser power (below 540 W). Rising of power leaded to full penetration and appearing of hemispheres on both sides, up and bottom. The bottom hemisphere was two times larger. By further increase of power and interaction time, the upper sphere happened to be solid inside, while before there were only hollow ones.

Table 10. Preliminary tests of laser processing of sample #1 with carbon-dioxide laser

Power, W	Time, s	Result (to naked eye)
270	0.5	Hemisphere on the top, size 0.5 mm
540	0.5	Hemisphere on the top, size 1-1.5 mm
810	0.5	Hemisphere on the top, size 1.5 mm Hemisphere on the bottom, size 3 mm
1080	1	Solid sphere on the top, size 2-3 mm Hollow sphere on the bottom, size 2-3 mm

The sample # 3 (SiO_2 49%, Al_2O_3 25%, Fe_2O_3 13%) revealed tiny spheres. Low energy input provided upper sphere (270 W), higher energy (up to 810 W) input made an upper melt and tiny bottom sphere.

Table 11. Preliminary tests of laser processing of sample #3 with carbon-dioxide laser.

Power, W	Time, s	Result (to naked eye)
270	0.5	Sphere on the top, size 0.5 mm
540	0.5	Melt on the top
810	0.5	Melt on the top, tiny sphere on the bottom
270	1	Melt on the top, tiny sphere on the bottom, size 1 mm

The sample #5 (SiO_2 53%, Al_2O_3 21%, CaO 9%) did not show any signs of glass sphere formation. Time of 0.5-1 seconds and power of 270-1350 W simply drilled the upper surface.

The sample # 6 (Al_2O_3 98%) revealed the spheres formation during relatively low power (270 W).

Table 12. Preliminary tests of laser processing of sample #6 with carbon-dioxide laser.

Power, W	Time, s	Result (to naked eye)
270	0.5	Sphere on the top, size 1.5 mm Sphere on the bottom, size 1.5 mm
135	1	Negative, only a dot
270	1	Sphere on the top, size 2 mm Large melt on the bottom
270	2	Sphere on the top, size 1 mm Large spherical melt (solid) on the bottom, size 3-4 mm in width

After the first trials following thoughts were concluded. Switch to IR wavelength (1.064 μm) provided the same effect of glass sphere formation. But CO_2 laser tended to drill through the material, consequently spheres/ hemispheres/melt frequently appeared on the bottom side (if under the sample was spare space). Also, the CO_2 wavelength interferes with glass, thus alleged glass spheres were destroyed by laser light between pulses. Obviously, that is why upper sphere did not occur in several cases.

Further experiments were conducted on three samples and recorded by camera with frequency of 500 frames per second. On snapshots interference of gas flow to unhardened glass spheres was clearly observed. Even without gas nozzle the flow was direct and blew growing melt. Nevertheless, in some cases spheres managed to expand, but slightly shifted to side.

The sample # 1 (SiO_2 72%, Al_2O_3 27%, Fe_2O_3 1%) with a glaze on bottom side, which was not an obstacle for laser beam.

Table 13. Video recorded tests of laser processing of sample #1 with carbon-dioxide laser

Power, W	Time, s	Upper sphere	Bottom sphere
270	0.50	Insufficient power. Upper melt is displaced to a side by air flow	
270	1.00	Insufficient power. Upper melt is displaced to a side by air flow	
540 (2 trials)	0.25	1. Hemisphere rises from 62 ms (2.4 in width and 1.3 in high) to a sphere (164 ms, 2 mm in diameter and 2.1 mm in high) 2. Finally, a bifurcated sphere at 174 ms 2.2 mm in width and 1.8 mm in high	1. Sphere shrinks to a hemisphere at 278 ms 1.3 mm in width and 0.5 mm in high 2. Sphere shrinks to a hemisphere at 586 mm 1.3 mm in width and 0.6 mm in high
540 (2 trials)	0.50	1. A melt is shifted to a side by air flow 2. A melt rises to a sphere at 102 ms 2.2 mm in diameter and 2.1 mm in high	1. Sphere shrinks to a melt 2. Sphere shrinks to a hemisphere

Table 13. Video recorded tests of laser processing of sample #1 with carbon-dioxide laser

540 (5 trials)	1.00	1. A melt rises to sphere at 300 ms (1.5 mm in diameter and 1.1 mm in high) 2. A hemisphere rises to sphere at 400 ms (1.8 mm in diameter and 1.3 mm in high) 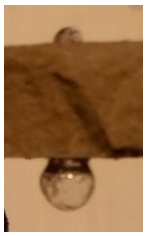 3. Hemisphere rises to sphere at 332 ms (2.0 mm in diameter and 1.6 mm in high) 4. A melt rises to a hemisphere at 438 ms (1.5 in width and 1.1 in high) 5. Hemisphere solidifies at 268 ms (1.4 in width and 0.7 in high)	1. Sphere shrinks to a hemisphere 2. Sphere at 988 ms (3.3 mm in diameter and 3.1 mm in high) 3. Sphere shrinks to a melt 4. Sphere at 734 ms (4.7 mm in diameter and 4.9 mm in high) 5. Huge double sphere approximately 6-7 mm in diameter and 3 mm in high 
540 (2 trials)	1.50	1. Melt rises to a sphere at 236 s (1.7 mm in diameter and 1.4 mm in high) 2. Melt rises to a sphere at 200 s (1.9 mm in diameter and 1.5 mm in high)	1. Sphere 4.9 mm in diameter 2. Sphere solidifies 728 ms 4.3 mm in diameter and 4.1 mm in high
810 (2 trials)	0.25	1. Melt rises to a sphere at 224 s (2.0 mm in diameter and 1.8 mm in high) 2. Melt rises to a sphere at 212 s (1.3 mm in diameter and 1.0 mm in high)	1. Melt 2. Melt shrinks to a hemisphere at 568 ms (1.6 in width and 0.8 in high)

Table 13. Video recorded tests of laser processing of sample #1 with carbon-dioxide laser

810 (2 trials)	0.50	1. Melt rises to a shifted hemisphere 2. Shifted melt	1. Sphere shrinks to a hemisphere 2. Sphere shrinks to a hemisphere
810 (2 trials)	1.00	1. Hemisphere and rises to a shifted sphere at 338 ms 2.8 mm in diameter and 2.5 mm in high 2. Hemisphere and rises to a shifted sphere at 306 ms 2.8 mm in diameter and 2.4 mm in high	1. Sphere shrinks to a hemispherical melt at 920 ms 2.1 in width and 1.8 in high 2. Sphere shrinks to a melt
1080 (2 trials)	0.50	1. Shifted melt 2. Shifted hemisphere	1. Sphere shrinks to melt, rises to a hemisphere 2. Sphere shrinks to melt, rises to a hemisphere at 680 ms 1.9 in width and 1.0 in high
1350 (2 trials)	0.50	1. Hemisphere at 286 ms 2.0 in width and 1.3 in high 2. Shifted melt	1. Sphere shrinks to a hemisphere at 524 ms 2.2 in width and 0.8 in high 2. Sphere shrinks to nothing
1620 (2 trials)	0.50	1. Shifted melt 2. Shifted sphere at 340 ms 1.2 mm in diameter and 0.9 mm in high	1. Sphere shrinks to a hemispherical melt 2. Sphere shrinks to a melt, rises to sphere, collapses and solidifies at 340 ms 3.7 mm in diameter and 3.2 mm in high
70 (2 trials)	0.50	1. Melt rises to a hemisphere at 190 ms 3.0 in width and 1.9 in high 2. Shifted hemisphere at 364 ms 0.9 mm in high	1. Melt 2. Elongated sphere at 510 ms 2.3 mm in diameter and 3.3 mm in high

Table 13. Video recorded tests of laser processing of sample #1 with carbon-dioxide laser

80 (2 trials)	0.50	1. Shifted sphere 2. Shifted hemisphere	1. Melt 2. Melt solidifies in hemisphere at 682 ms 2.4 in width and 1.8 in high
90 (2 trials)	0.50	1. Melt solidifies in a shifted sphere and hemisphere 2. Melt solidifies in a shifted sphere and hemisphere	1. Hemisphere at 586 ms 2.1 in width and 1.2 in high 2. Hemisphere at 678 ms 2.3 in width and 1.3 in high
2700 (3 trials)	0.50	1. Shifted melt 2. Shifted melt 3. Shifted sphere 	1. Melt 2. Melt 3. Melt rises to a sphere at 828 ms 3.7 mm in diameter and 2.5 mm in high

The expanded glass on the sample #1 severely undergone a gas flow, mostly all spheres, hemispheres, and melts were blown to side. Also, the material tended to produce large sphere on bottom surface than on upper surface. Perhaps due to hindrance of gas flow the size and shape of upper sphere suffered.

The power threshold was at 540 W of power and 1 second time of laser on. In case of these parameters on the upper side was a hemisphere approximately 1 mm in high, on the bottom side was a sphere 3-7 mm in diameter. During 540 W laser power and 1.5 second of laser action the upper hemisphere reached 1.5 mm in high, while bottom sphere was 4-5 mm in diameter. The increase of power up to 810 W avoided spheres on bottom side but provided spheres on upper side 1-3 mm in diameter. Further enhance of power resulted generally in melt or hemisphere. Thus, the optimal parameters for sphere formation were 540 – 810 W of power and 1-1.5 seconds of irradiation.

The sample # 3 (SiO_2 49%, Al_2O_3 25%, Fe_2O_3 13%) was studied in detail. Below listed results regarding consistently changed power:

Table 14. Video recorded tests of laser processing of sample #3 with carbon-dioxide laser.

Power, W	Time, s	Upper sphere	Bottom sphere
270	0.5	A melt	A melt rises to a sphere, collapses and solidifies in hemisphere at 394 ms 1.3 mm in width and 0.7 mm in high
540 (2 trials)	0.5	1. A melt 2. A melt	1. A melt rises to a hemisphere at 296 ms 1.3 mm in width and 0.7 mm in high 2. Nothing
810 (2 trials)	0.5	1. A melt rises to a hemisphere at 158 ms 0.8 mm in width and 0.7 mm in high 2. Sphere at 0 ms 1.0 mm in width and 0.7 mm in high	1. A melt rises to a hemisphere at 158 ms 0.9 mm in width and 0.5 mm in high 2. Nothing
1080, 1350, 1620, 1890, 2160, 2430, 2700	0.5	A melt	A melt

The sample did not show appropriate results regarding spheres formation during experiments.

The sample # 6 (Al_2O_3 98%, thickness approximately 4.25 mm):

Table 15. Video recorded tests of laser processing of sample #6 with carbon-dioxide laser.

Power, W	Time, s	Upper sphere	Bottom sphere
270	0.10	Sphere rises after the end of laser radiation during 70 ms from hemisphere (1.5 mm in width and 0.5 in high) up to 1.2 mm in diameter and 1 mm in high	No
270	0.25	Hemisphere rises after the end of laser radiation during 14 ms and blows fluctuates a little and solidifies (1.5 mm in width and 0.8 in high)	Hemisphere rises after the end of laser radiation, fluctuates, blows and solidifies after 40 ms from the end of laser radiation (0.9 mm in width and 0.3 in high)
540 (3 trials)	0.50	Sphere fluctuates and shrinks to small hemisphere	Sphere fluctuates and shrinks to small hemisphere
810 (3 trials)	0.50	1. Hemisphere rises after the end of laser radiation during 148 ms up to 2.2 mm in width and 1.3 in high 2. Hemisphere rises and shrinks 3. Hemisphere rises after the end of laser radiation during 186 ms up to 2.4 mm in width and 1.3 in high	1. Finally, a melt 2. Finally, a melt 3. Hemisphere fluctuates and solidifies after 186 ms from the end of laser radiation (1.6 mm in width and 0.9 in high)

Table 15. Video recorded tests of laser processing of sample #6 with carbon-dioxide laser.

1080 (3 trials)	0.50	1. Finally, a melt 2. Finally, a melt 3. Hemisphere fluctuates, shrinks and starts to rise from melt at 98 s after the end of laser radiation (2.1 mm in width and 0.3 in high) up to the sphere during 54 ms (2.7 mm in diameter and 1.8 mm in high)	1. Finally, a melt 2. Finally, a melt 3. Sphere fluctuates and finally becomes a hemisphere at 414 after the end of laser radiation (1.8 mm in width and 1 in high)
1350 (3 trials)	0.50	Finally, a melt	The melt 2-3 times starts to expand but shrinks 1. Finally, a hemisphere at 136 ms after the end of laser radiation (1.3 mm in width and 0.5 in high) 2. Finally, a melt 3. Finally, a melt
1350	1.00	Close to end hole is already drilled, so beam does not interact with surface. Occurs a melt around hole	After the end on bottom begins to rise hemisphere from the melt inside (non-visible part) during 18 ms up to 1.5 mm in width and 0.8 in high
1620	0.50	Finally, a melt	Finally, a melt
1890	0.50	The excellent round hole was drilled	
2160	0.50	Finally, a melt	Small hemisphere on the bottom begins to grow after radiation up to 1.3 mm in width and 0.9 in high
2430	0.50	Small amount of melt on the up edges (the hole is obviously visible)	Small melt at the bottom, but it is not a hindrance to see through

Table 15. Video recorded tests of laser processing of sample #6 with carbon-dioxide laser.

2700	0.50	Nothing on the top	Finally, a hemisphere at 422 ms after the end of laser radiation 2.2 mm in width and 0.8 in high

The experiment showed the obvious excess of laser power for the sample # 6 in order to produce a sphere. The low power 270 W and short time 0.1 s provided a sphere 1.2 mm in diameter and 1 mm in high. Also, the 1080 W power and 0.5 s produced a sphere 2.7 mm in diameter and 1.8 mm in high, but other two trials with the same parameters made only a melt. After increase of energy input the material tended to produce only hemispheres (expanded melt after the end of laser radiation). In further of power higher than 1350 W the material was drilled through.

2.8 Optical properties of sample and spheres.

The transmittance of a sample was estimated by power counter Gentec-EO SOLO 2. It was found that ceramics of 7 mm thickness transmitted maximum 0,5 - 1% of power of laser beam. Thus, according to the Lambert-Ber's law (Equations 7-8) the absorption coefficient α was approximately 690 m^{-1}.

$I = I_o e^{-\alpha x}$ (Equation 7)

or

$P = Pe^{-\alpha x}$ (Equation 8)

Figure 42. Universal measuring tool of energy and power of laser radiation Gentec Solo PE-2: power range 0,001-110 W, spectral range 0,19-11μm, aperture 19 mm.

Using spectrophotometer (Fig. 43) the transmission and reflection of glassy spheres were defined in the visible and near IR ranges. It was found that the optical properties of the spheres in the selected range were mostly neutral.

Figure 43. Microscope-spectrophotometer LOMO MSFU-K: range of spectral reflection 350-900 nm, range of diffuse reflection 380-760 nm, transmission range 350-900 nm, spectral range of luminescence 400-700 nm, magnification 50x-1000x, the minimum size of studied spot 1 μm.

Experiment with the solution of gold nanoparticles was studied by the same microscope-spectrophotometer. Instead of water the surface of the ceramic was moistened with a solution containing Au nanoparticles. Initially, it was assumed that nanoparticles could become embedded in the walls of the sphere. However, the spectra showed the absence of extra elements. It was identical to the spectra obtained previously with water experiments.

2.9 Thickness measurements the spheres

To measure the thickness of spheres they were carefully detached from the surface and shattered into pieces. The samples were studied using optical microscope (Fig. 44) and interference method.

Figure 44. Universal microscope Axio Imager A1.m: magnification 100x-1600x, resolution (at least) 3800 lines per mm.

The samples were studied using optical microscope and interference method. To implement the method the microscope is switched in reflected light mode for observation interference pattern from light with circular polarization. Height of the sample is determined in accordance with the following formula:

d = $\frac{n\Delta}{2} = \frac{\lambda b}{2a}$ (Equations 9),

d – height of the test specimen,

n –refractive index of the environment (usually n=1),

Δ – path difference,

a – distance between interference stripes,

b – shift of interference stripes on the specimen,

λ – wavelength of the illuminating light (550 nm).

Computer identifies values ‘a’ and ‘b’. In that way the two measuring conducts: distance between interference stripes on the ceramic specimen and on the twofold image of sphere's shard (Fig. 45). Then the subsequent calculation according to updated formula is made (Equations 10), the final obtained value is the thickness of sphere's wall ‘d’ in nm.

d = $\frac{\lambda \cdot b \cdot k}{2a}$, (Equations 10)

k – coefficient for microscope lens. In the present case 10x/0.25 k=0,0161

Distances are dependent on the aperture and decrease with increasing aperture lighting. Formula is adjusted for a particular lens by means of the coefficient ‘k’. The coefficient is selected from tabular values, which are taken from guidance on the use of the microscope Axio Imager A1.m.

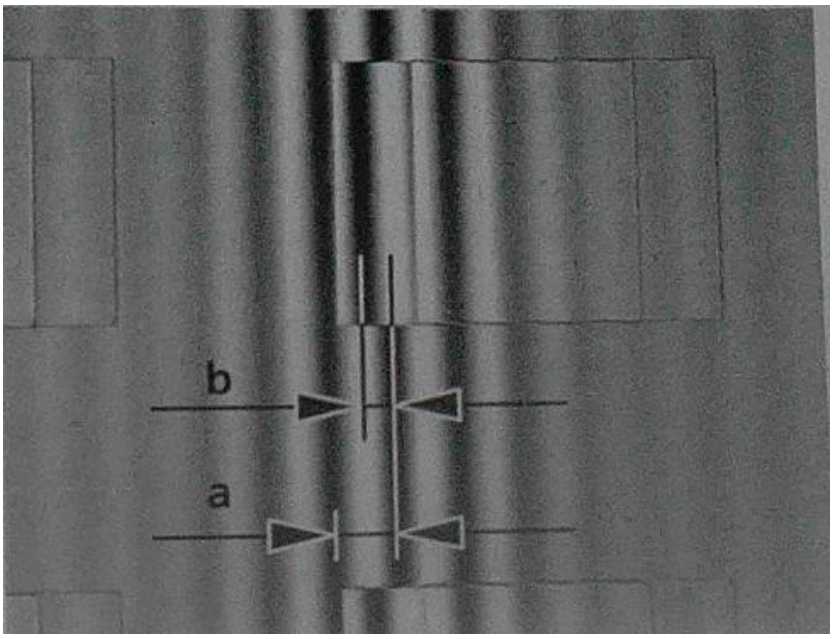

Figure 45. Sketch of interference pattern. ‘a’ – interference distance, b – the distance which shifted interference stripe due to reflection in the plate, in our case, a shard of the sphere.

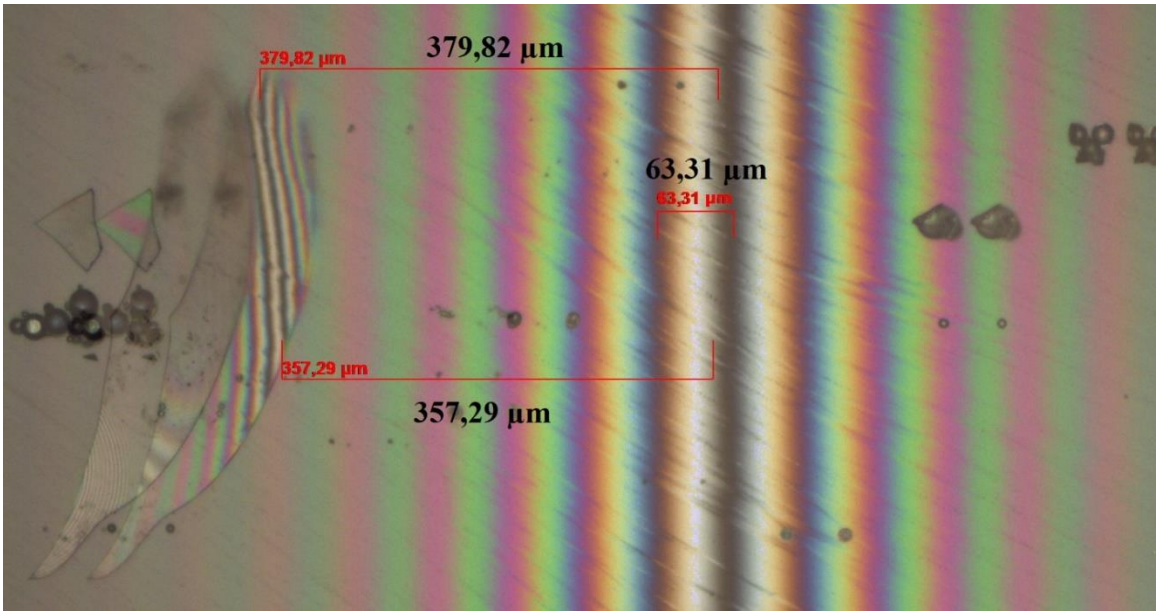

Figure 46. The interference pattern on the shards of the sphere.

It was supposed that wall thicknesses of spheres are thinner at the top and thicker at the bottom. But the assumption was not confirmed due to the large data scatter. As a result, thickness range was from 0.1 to 1 microns, independently from radiation parameters. Figure 47 shows a graph of the dependence of wall thickness on the power.

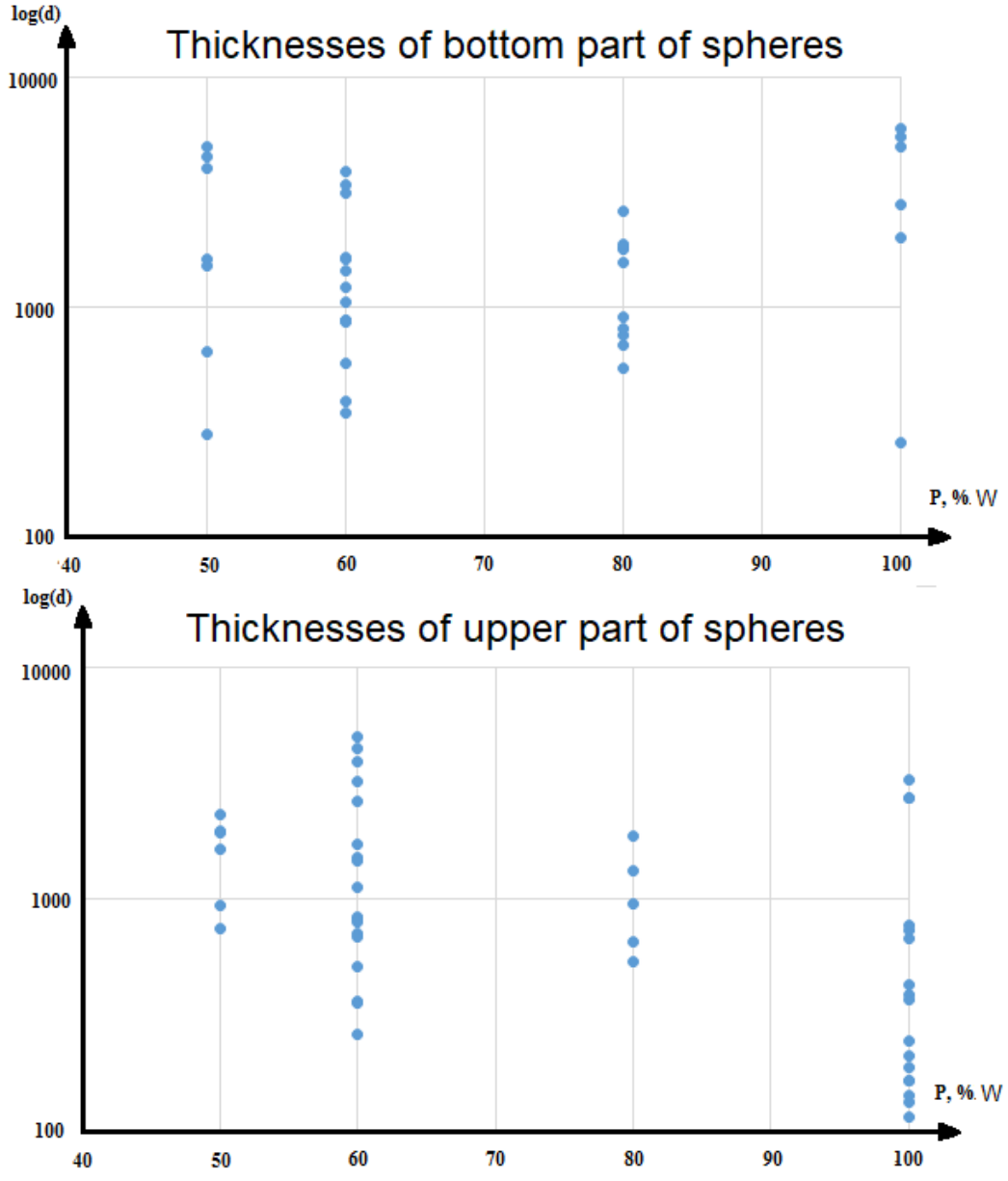

Figure 47. The spheres' wall thickness.

2.10 Size distribution of ejected microspheres

During ablation process in addition to the evaporation the ejection of splashes happened from a molten bath. These splashes further formed microspheres on the surface of glass plates, which were installed to collect them. Production of microspheres was carried out on the #2 at different pulse repetition frequencies on a dry sample and in the presence of liquid.

Size distribution of these particles approximately from 3 up to 7 micro meters and size was not in correlation with laser frequency. The presence of water leaded to the appearance of particles up to 60 microns, which was not observed during dry ablation.

2.11 Thermal imaging monitoring of the process

Thermal camera Flir Titanium 520M was applied for observation the processes of ablation and spheres' growth on the sample #1, which undergone near IR laser radiation.

Figure 48. Thermal camera Flir Titanium 520M: spectral range 3-5μm, minimum image resolution 320x256 / 14-bit, maximum refresh rate of full frame 380 Hz, maximum refresh rate of frames with a minimum resolution 20 kHz, integration time 3 ms.

Using a thermal imaging camera, the cooling rate of the sphere was evaluated. According to the averaged results, cooling rate of spheres' bottom was approximately 100 K/s, central part - approximately 240 K/s, top - approximately 400 K/s.

The thermal camera offers an opportunity to monitor the change of temperature field. However, the camera cannot catch the suitable range, so it is assumed that temperature reaches 2500-3000

kelvin degree. Sphere's cooling fits in the Newton's-Richman's law - as the heat flow from the sphere to surrounding air environment.

Combined thermal dynamics from recordings of six experiments (range of thermal camera varied) is presented on the line chart (Fig. 49). The fixation points of temperatures served the hottest spots on captured videos from thermal imaging camera. In other words, they were points which located in the place where the focused laser radiation shoot. In these experiments, the cooling process started after the end of laser exposure. While in experiments with impulse laser treatment temperature decries between pulses. Unfortunately, the real temperature is higher than the recorded temperature, therefore it can only be assumed that ceramics heated up to 3000 K due to limited range of thermal camera.

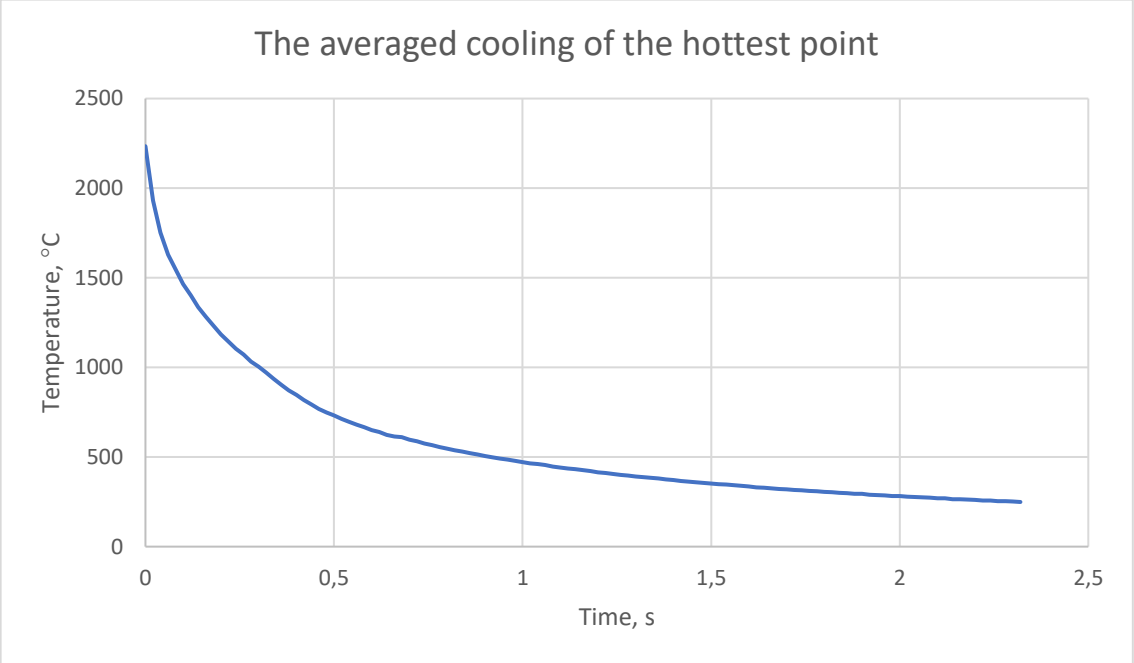

Figure 49. Combined line graph of cooling the spot of very laser irradiation (cw regime, sample #1).

Experiments with pulse laser showed another outcome. Ceramics heated up to 1750 °C in the best-case scenario and up to 1000-1500 °C in other cases. Besides, in recorded experiments temperature fluctuated around maximum achieved temperature. All experiments were negative regarding sphere formation. Consequently, sphere emergence demands temperature at least above 1750 °C. Combined thermal dynamics from recordings of seven experiments (pulse regime) is presented on the line chart (Fig. 50).

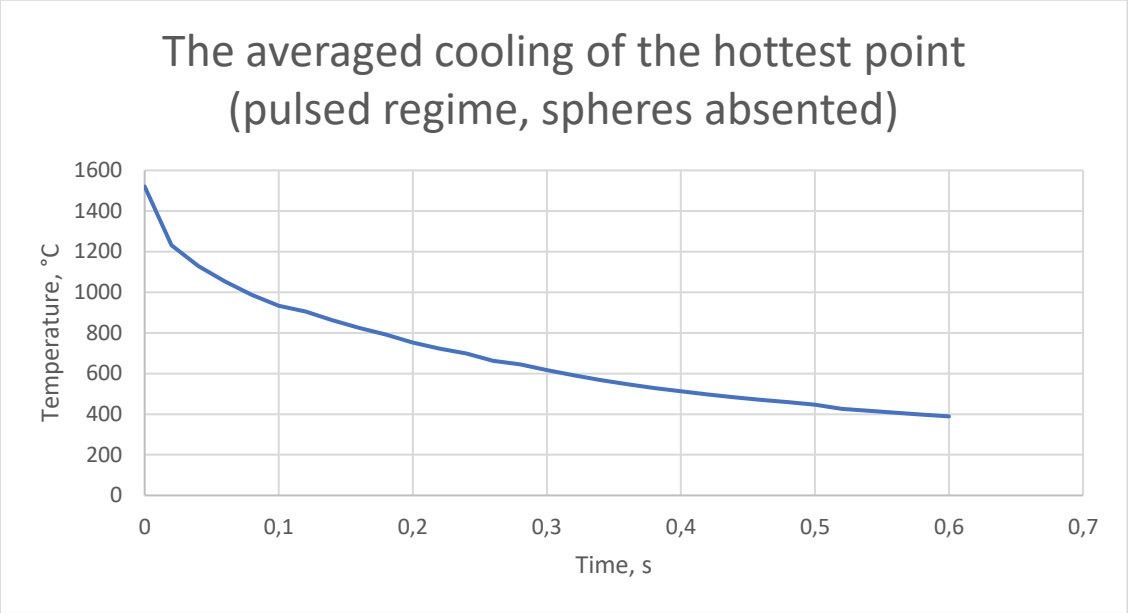

Figure 50. Combined line graph of cooling the spot of very laser irradiation (pulsed regime, #1).

The cooling process roughly obeyed to logarithmic law. The general tendency coincided with the theoretical Newton's-Richman's law, but the cooling rate was more gradual. Probably, it was due to warmth from molten bath.

The threshold power density required for the formation of the spheres are 12 GW / m^2 for continuous laser exposure and 4 GW / m^2 for pulsed laser exposure, when the temperature reached about 1600 K. The temperature of the irradiated sample reaches 2350 K during 10 kW / m^2 of impulse laser exposure and 2540 K during 40 GW / m^2 of continuous laser exposure.

2.12 Electron microscopy of spheres

SEM-images from the electron microscope MERLIN Zeiss SEM (InLens and SE2 secondary electron detectors at 15 kV) (Fig. 50-51) and EDX-analysis allowed to obtain data on the properties of sample. The chemical composition of the original ceramics sample #1 was detected by EDX analysis: approximately 72% SiO_x, 27% AlO_y, and less than 1% FeO_z. While sphere consists of 61% SiO_x and 37% AlO_y. There are negligible quantities of Na, Mg, K, etc., which may be due to dust left by fingerprints and irregularities of surface.

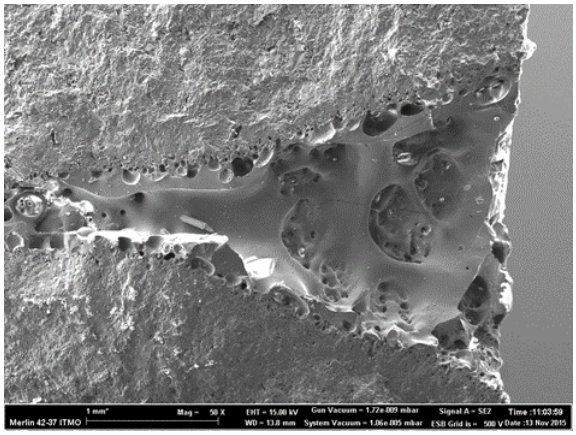

Figure 50. Cross-section SEM-image the crater on sample #1 (Sinev et al. 2016, p. 546).

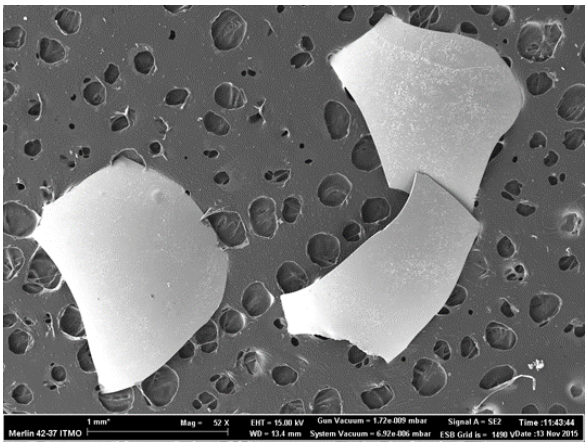

Figure 51. SEM-image of glass sphere shards (Sinev et al. 2016, p. 546).

2.13 Hardness testing of samples

To measure the glass sphere hardness was used Hardness testerPMT-3M. The diamond tip with 30 grams left an ovoid mark estimated 400 and 600 micro meters on top of the ball, which is equivalent to 0.2 Newton per square meter of hardness (Fig. 52-53).

Figure 52. Hardness test experiment of the sample #6.

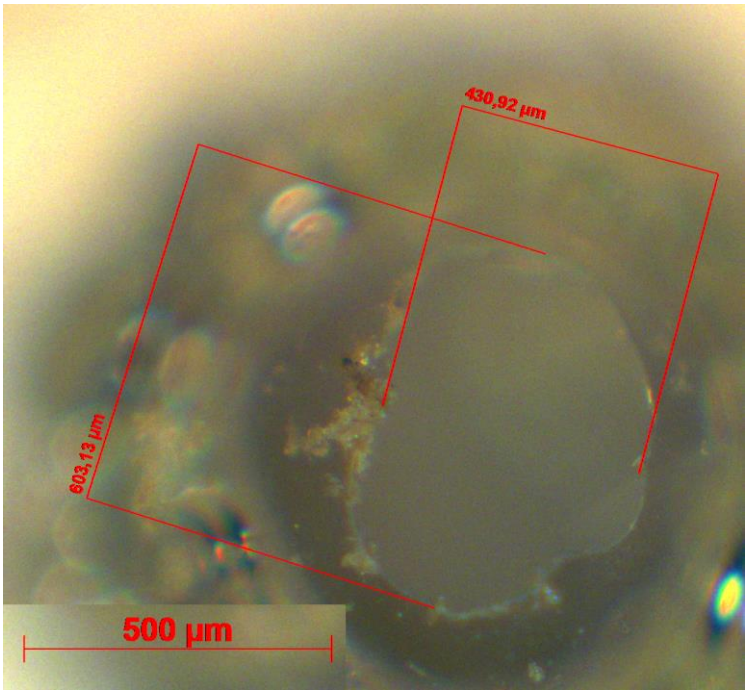

Figure 53. Hole obtained on the sample #6 after the determination of hardness.

Threshold value of the load applied normally to the top of the sphere was determined, it was about 5 mN.

2.14 Explanation of the glass sphere formation above crater

Before the laser processing a thin distilled water layer is applied on ceramic sample's surface. Water quickly penetrates into pores but does not flow through it. The rate of penetration depends on the composition and porosity of samples. In case of previously irradiated samples, which are warmer than the environment, the water from the surface evaporates faster. At the moment of exposure, the material melts in the impact zone, forming a cone-shaped melt zone inside and inflated melt outside.

The melt takes the form of a sphere due to the expansion of the material from heating. The radius and height of the flaming sphere can be from 0 to 1-2 mm. Part of the material is ejected as a result of ablation. But the water (vapor) in pores under the impact zone remains there, and only when the laser radiation is switched off the vapor pressure blows out the melt, forming a sphere. Experiments with broken spheres can be explained by the excess of vapor force over the forces of surface tension, viscosity (in the case of not solidified sphere) and air pressure. Also damage from laser beam (when the sphere is trying to grow before the end of exposure), and the excess of vapor over the surface tension forces of the frozen sphere (fragility, thickness) affect the sphere.

When pulsed laser action with a low pulse frequency, in the intervals between them, the sphere is constantly trying to grow, but unsuccessfully resists the current laser radiation. With continuous exposure, the oscillations of the melt bath are much smaller. And at high pulse rates, the camera cannot catch all the pulses, and the shots shows obvious melt's attempts to raise into a sphere, and sometimes only slight fluctuations in the melt are visible. In the interval between pulses, the heat goes inside the sample, as a result, the reached temperature in the center of the irradiated area is less than at the same power, but continuous mode.

Inflated by water vapor, the sphere aims to reduce the area of its surface to the minimum possible sizes at a given volume (the force of surface tension). As the temperature increases, the surface tension coefficient decreases.

2.15 Modeling of formation of a thin-walled sphere from a cooling melt

In this chapter modeling of melt blowing of silicon oxides and aluminum oxides by evaporating water is presented. The following assumptions were made to simplify the calculations:

- The material of the ceramics sample is homogeneous
- The melt is homogeneous, and the sphere inflates equally in all directions
- Heat capacity and heat transfer coefficient do not depend on temperature
- The temperature to which the melt is heated is taken to be 3000 K without preliminary calculation

Approximately estimated parameters (Ϭ, C, η, α)
Ϭ - surface tension coefficient
C - total heat capacity of the melt mass
η - dynamic viscosity of the melt
α - heat transfer coefficient

The material is heated to the melting point by laser radiation, the melt depth increases to several millimeters, forming a cone, the melt above the hole forms a small bulge. At the end of the last laser pulse, the water vapors under the treatment zone are released and go upward. The melt begins to cool and expand.

2.15.1 First subtask. The inflating sphere law.

Based on the videos shot with the help of a high-speed camera (500 frames per second), the volume of the sphere increases on average by logarithmic law. Take the following data: melt volume after 0.002 seconds from the end of exposure is 0.02 m3, melt volume after 0.2 seconds from the end of exposure is 0.5 mm3 (Fig. 54).

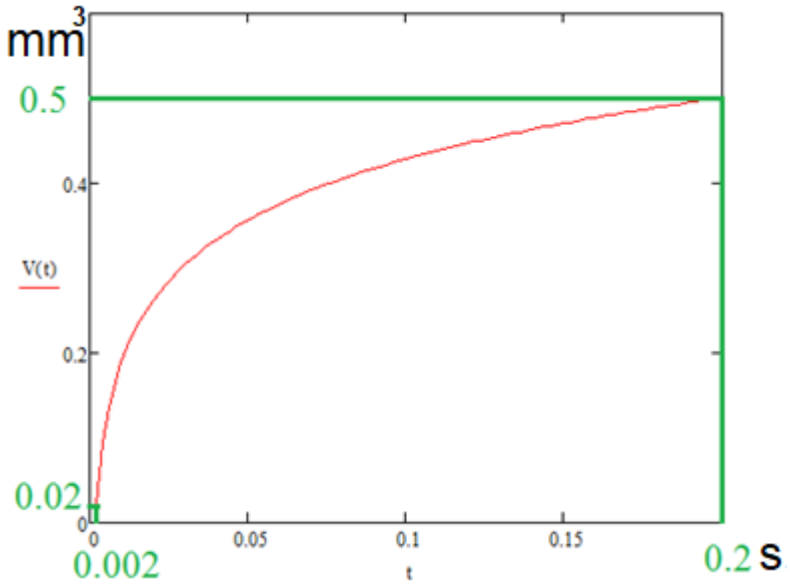

Figure 54. Logarithmic graph of inflating sphere.

So, the increase occurs according to the law:

$V(t) = 0.104 \cdot \ln(t) + 0.668$, (Equation 11)

Where [V] = mm3, [t] = s.

Express the radius of the sphere from the volume by the formula of the ball, ignoring the fact that up to a certain blow-up the formula cannot be used $V = 4/3\ \pi\ R^3$ (because before the height is equal to the half-width of the melt should be used V = 1/6 π H3 + ½ π h r2).

$r(t) = (3*V(t) / 4\ \pi)^{1/3}$ mm (Equation 12)

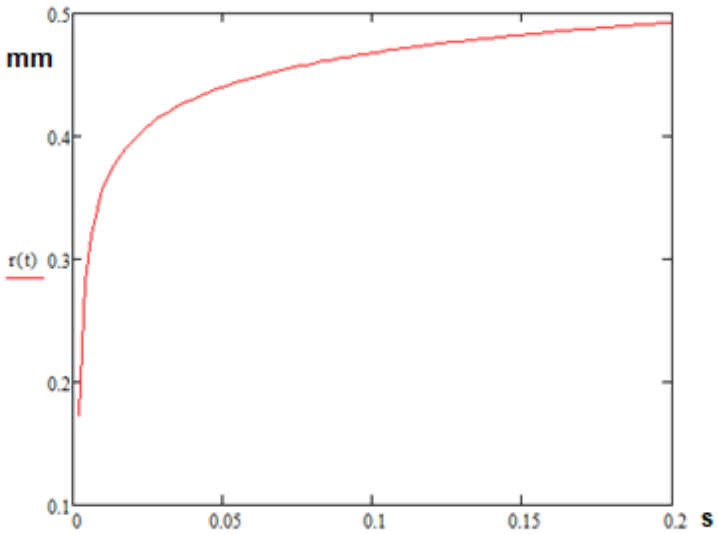

Figure 55. Radius of inflating sphere.

2.15.2 Second subtasks. The law of sphere cooling.

Consider the problem of the cooling of the sphere as a heat flux from the inflating sphere to the ambient air (Newton-Richman's law), directed perpendicular to the surface. The temperature tends to the surrounding temperature by exponent law:

$T(t) = T_{out} + e^{-kt}(T_0 - T_{out})$ (Equation 13)

The ‘k’ coefficient has the following dimension: $[\frac{\mathrm{W}}{\mathrm{m}^2 * \mathrm{K}} * \mathrm{m}^2 * \frac{\mathrm{K}}{\mathrm{J}} = \frac{1}{\mathrm{s}}]$. Heat transfer coefficient α $[\frac{\mathrm{W}}{\mathrm{m}^2 * \mathrm{K}}]$, S [$m^2$] - surface area of the expanding sphere, c $[\frac{J}{\mathrm{K}}]$ - the total heat capacity of the melt mass in question.

In general, the heat transfer coefficient α is calculated and determined experimentally and depends on the temperature difference and surface geometry. But in present work the fact that α function is neglected, and α is taken as a constant.

Express the surface area through the radius (division by 1000 to compensate for the radius expressed in mm):

$S = 4 \cdot \pi \cdot (r(t)/1000)^2\ m^2$ (Equation 14)

Estimate the specific heat capacity of the material composition:

$c = c_1 * \%_1 + c_2 * \%_2$, where $\%_1$ – part of SiO2, $\%_2$ – part of Al_2O_3 (Equation 15)

c = 1200*0.6 + 1100*0.4 = 1160 kJ/kg*K

By multiplying the specific heat by the melt mass at the initial time, we obtain the total heat capacity:

$C_{total} = c*m = c*V_{initial}*\rho = 1160*0.02*10^{-9}*2300 = 53.36$ [J/K] (Equation 16)

$V_{initial}$ - $0.02*10^{-9}$ – the amount of the initial melt [m^3]

ρ - 2300 – the approximate density of the melt [kg/m^3]

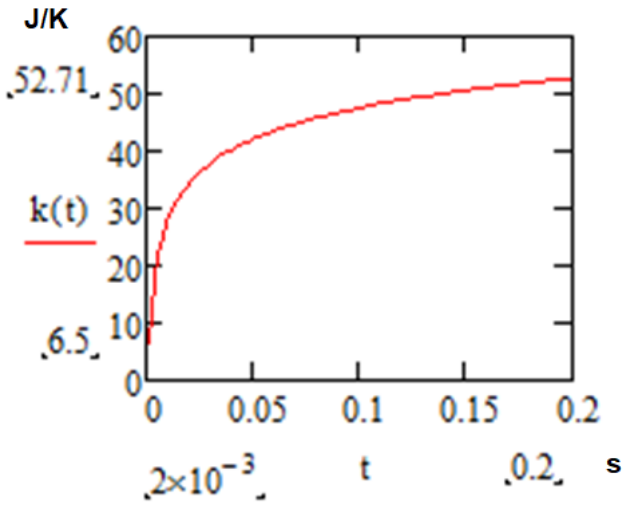

Figure 56. The graph of 'k' coefficient.

Thus, the law of cooling:

T(t) = 293 + exp(-k(t)*t)*(3000-293)

$\alpha = 10^9$ – selected

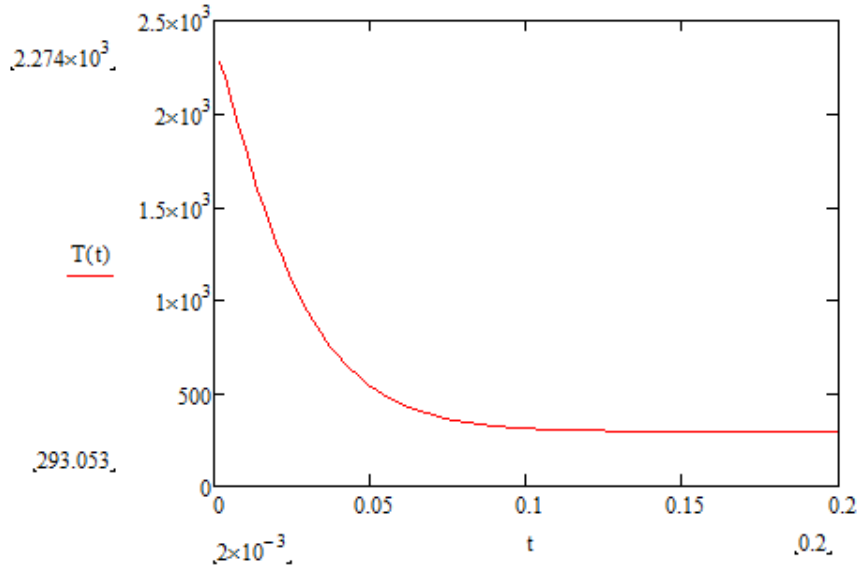

Figure 57. Cooling according to Newton's-Richman's law.

When water vapors displace the melt to the top, the air pressure force, the surface tension and viscosity stop the volume increase process. Write the equation of equilibrium of forces at the end of inflation (0.2 seconds):

$P_{\text{water vapor}}(t) = P_{\text{air}} + P_{\text{viscous friction}} + P_{\text{surface tension}}$ (Equation 17)

2.15.3 Third subtasks. The surface tensions.

First, calculate the surface tension coefficient:

$\sigma = \sigma_{SiO2} * \%_1 + \sigma_{Al2O3} * \%_2 = 0.29*0.6 + 0.58*0.4 = 0.406$ N/m (Equation 18)

where $\%_1$ – part of SiO_2, $\%_2$ – part of Al_2O_3

Surface tension pressure of the outer surface of the sphere (division by 1000 to compensate for the radius expressed in mm):

$P_{\text{surface tension 1}}(t) = 2 * \sigma * 1000 / r(t)$ Pa (Equation 19)

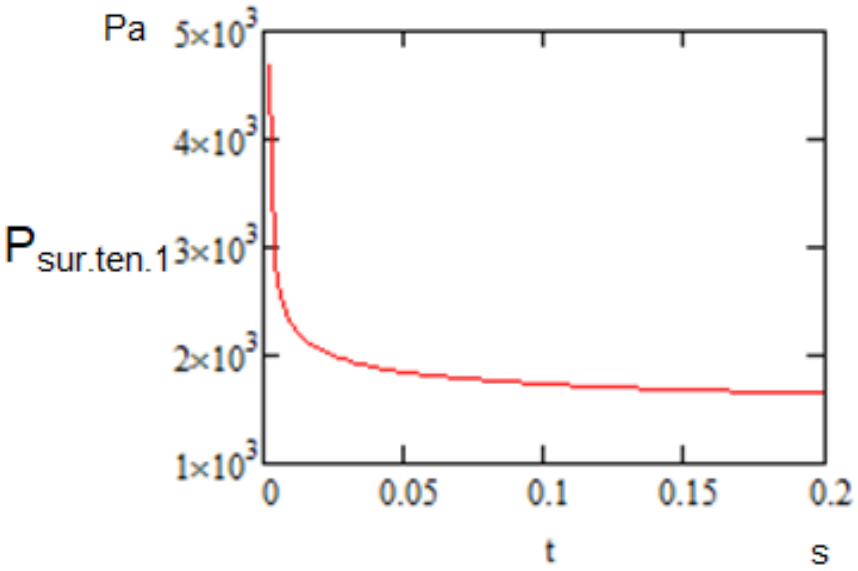

Figure 58. Surface tension pressure of external sphere surface.

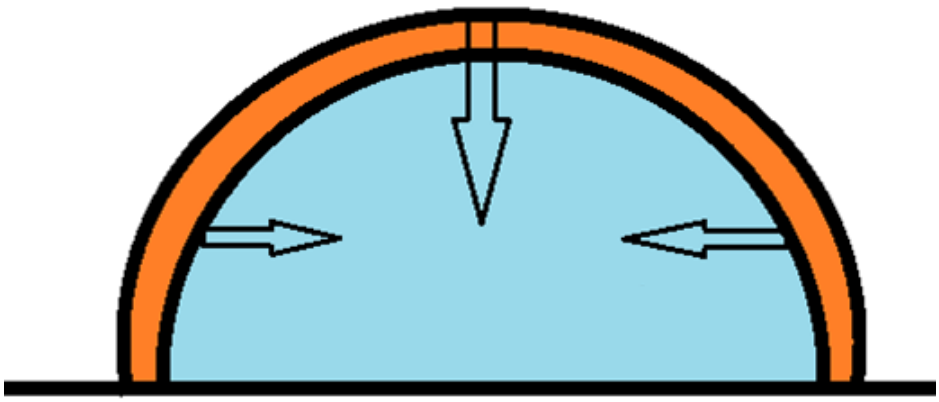

Figure 59. Scheme of external and internal surface tension pressures.

To calculate the surface tension pressure of the inner surface of the sphere, express the radius of the inner spherical surface:

$V_{empty} = V(t) - V(0.002)\ mm^3$ (Equation 20)

$r_{empty}(t) = (3 * V_{empty} / 4\ \pi)^{1/3}\ mm$ (Equation 21)

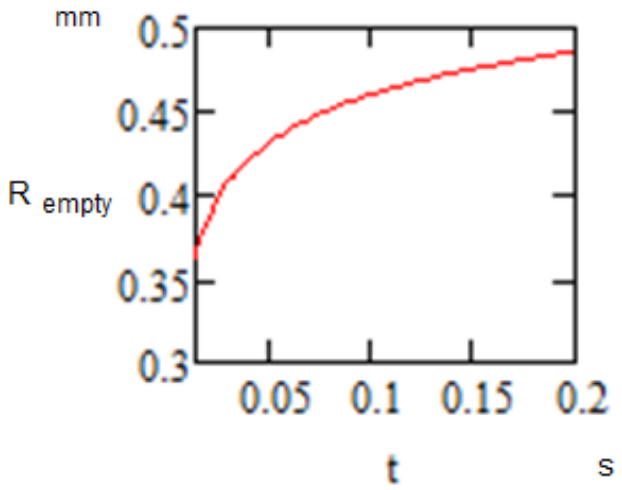

Figure 60. Radius of internal sphere surface.

Also estimate the thickness of the walls of the sphere, assuming that they are always equal to the thickness:

$h(t) = r(t) - r_{empty}(t)$ (Equation 22)

$h(0.2) = 6.6\ \mu m$

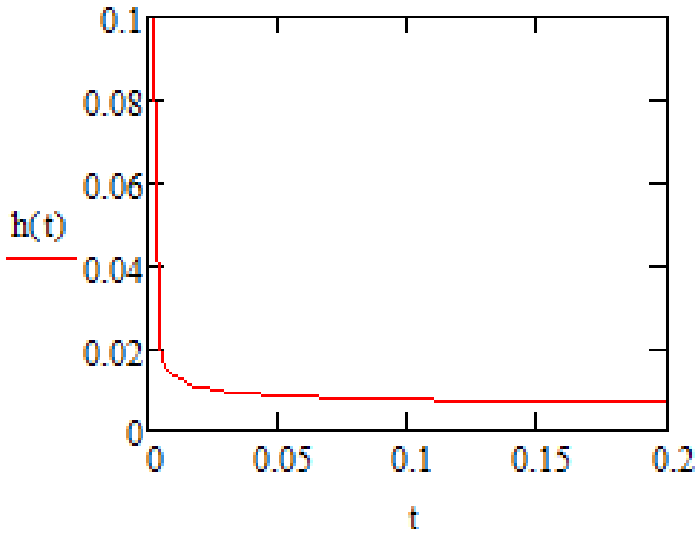

Figure 61. Sphere thickness.

$P_{surface\ tension\ 2}(t) = 2 * Ϭ * 1000 / r_{empty}(t)$ Pa (Equation 23)

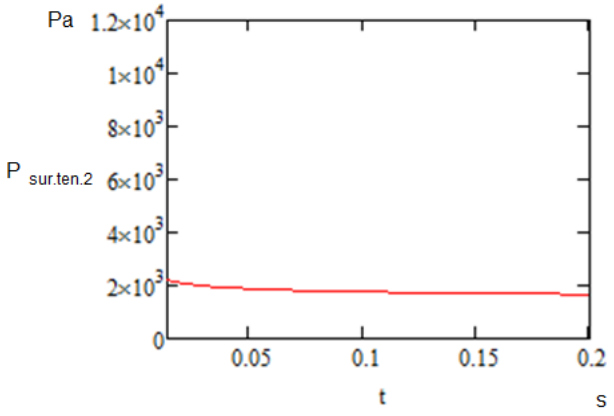

Figure 62. Surface tension pressure of internal sphere surface.

Now add up the two tension forces:

$P_{surface\ tension}(t) = P_{surface\ tension\ 1}(t) + P_{surface\ tension\ 2}(t)$

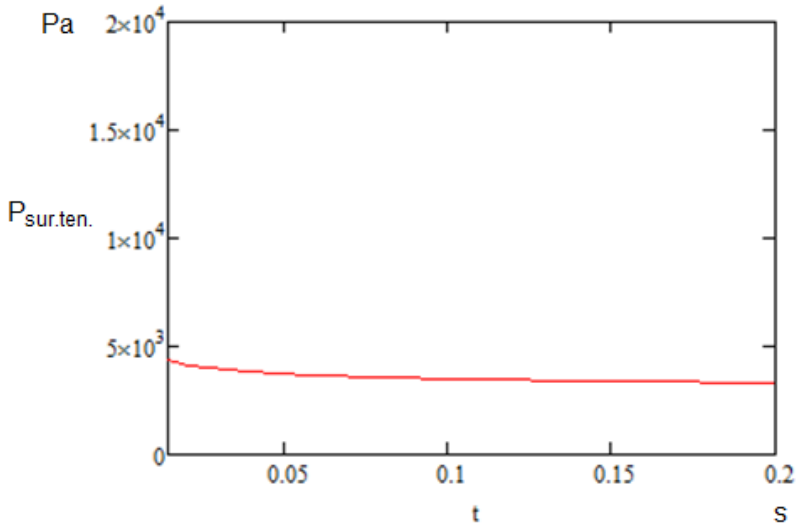

Figure 63. Total surface tension pressure sphere.

2.15.4 Fourth subtask. Viscous friction resistance

This subproblem is solved the most roughly, considering the inability to establish the values of the coefficient of viscosity, as well as the possible error in the choice of the general formula. Consider the general formula of viscosity:

$F = 6\pi r\eta v$, (Equation 24)

Where F – force of viscosity, r – sphere radius, η - dynamic viscosity, ν – speed of radius increase.

The speed of radius increase:

ν(t) = dr(t)/dt mm/s (Equation 25)

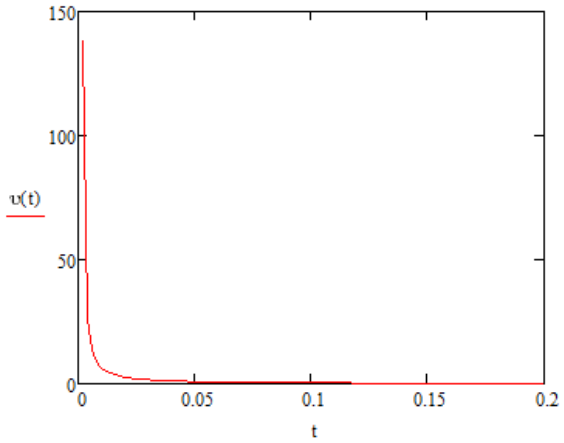

Figure 64. Speed of sphere expansion.

The viscosity of amorphous materials is close to 0 at such high temperatures, and in the glass-like state the viscosity reaches 10^{11}-10^{12} Pa*s. Express the dependence of η from the time:

η(t) = 1.1 * 10^5 * exp(30*t) - selected, given the subsequent equality of forces

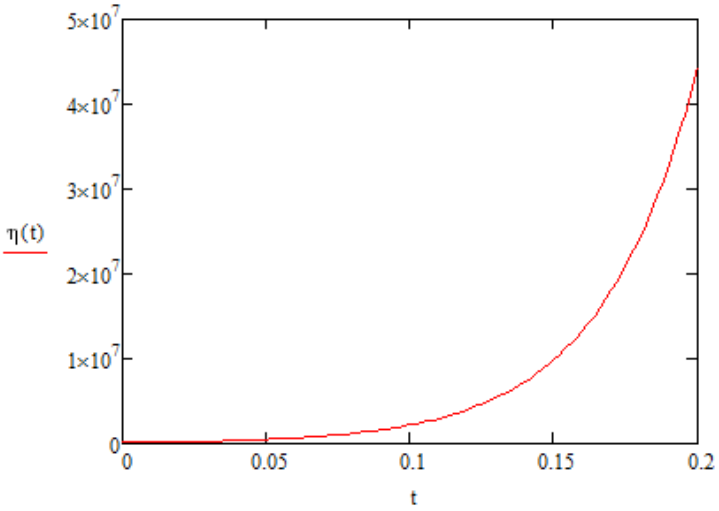

Figure 65. Viscosity of heated glass.

Equivalent to the pressure resistance of viscous friction:

$P_{viscousity} = 6*\pi*r(t)*10^{-3}*\eta(t)*\nu(t) / 4*\pi*(r(t)*10^{-3})^2$ (Equation 26)

$P_{viscousity} = 3*\eta(t)*\nu(t) / 2*r(t)*10^{-3}$ (Equation 27)

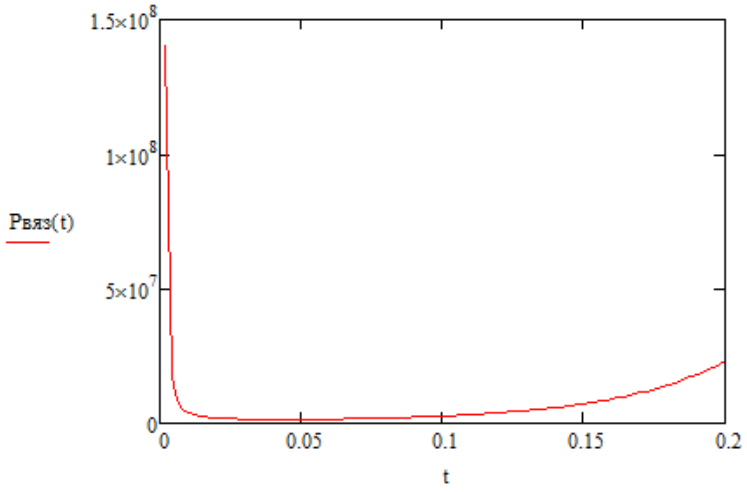

Figure 66. Viscosity friction of heated glass.

2.15.5 Fifth subtask. The water vapor pressure

The amount of vapor in the pores of the material under melt (porosity of 11%, the depth of the cylinder is equal to the specimen thickness minus the depth of the melt, the radius of cylinder is 0.5 mm):

$V \approx \pi * (5*10^{-4})^2 * 4*10^{-3}*0.11 = 3.5*10^{-10}\ m^3$ (Equation 28)

$\rho_{overheated\ vapor} = 201.7$

$P_{water\ vapor}(t) = \nu RT/V = mRT/MV(t) = V\ \rho_{overheated\ vapor}\ RT/MV(t)$ (Equation 29)

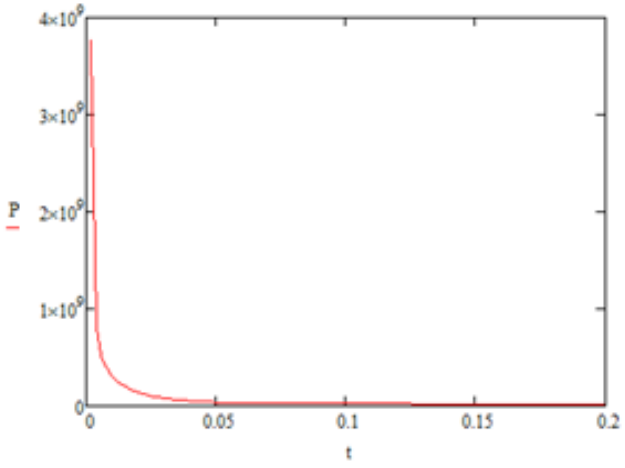

Figure 67. Pressure of water vapor.

Let's go back to the beginning of the third subtask and make sure that the forces come to equilibrium in ≈ 0.2 seconds:

$P(t) = P_{\text{water vapor}}(t) - P_{air} - P_{\text{viscosity}} - P_{\text{surface tension}}$ (Equation 30)

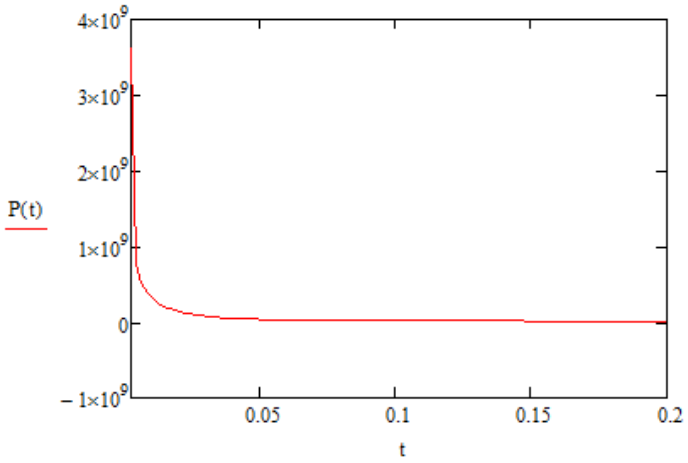

Figure 68. Total pressure.

$P(0.2) = -1.99*10^6$

$P(0.195) = 7.163*10^5$

Thus, the selection of α and η solved the problem of cooling and forces causing an increase in the radius of the sphere. The parameters of the material were taken approximately, the averaged process time and volume dynamics were taken from the results of experiments on the Mini Marker 2, at maximum power, the exposure time of 1 second.

4 CONCLUSION

Master thesis studied the laser ablation of ceramics. Laser processing was water-assisted, two pulsed lasers with 1.07 μm wavelength, one cw laser with 1.07 μm wavelength and one pulsed laser with 10.6 μm wavelength were used. Six ceramics materials with different chemical composition were investigated regarding to peculiarity of laser processing. The effect of glass sphere formation from melt above crater was observed. This effect was explained by water vapor pressure, which pushes the melt. The dynamic model of active forces, such as vapor pressure force, surface tension and viscosity, was described and calculated approximately. Dynamic viscosity coefficient ($\eta(t) = 1.1 * 10^5 * \exp(30*t)$ changes from 0 to $4.5*10^7$ Pa*s) and heat transfer coefficient ($\alpha = 10^9$ W/m^{2}K) were estimated in relation to the rest combined forces and sphere expansion mechanism. The problems of sphere expansion, cooling, surface tension, viscosity and vapor pressure were solved.

By thermal imaging monitoring was defined temperature of melt, it reached 3000 K. Size distribution of bath debris ejected during different frequencies did not show correlation with laser parameters and was approximately from 3 up to 7 micro meters. The chemical composition of sample #1 was examined by EDX-analysis. It revealed 72% of silicon oxide and 27% aluminum oxide. While aluminum oxide in sphere composition increases up to 37%. Optical spectrums showed neutral result of spheres, even in case of Au-nanoparticle solution used as liquid assistant.

The hardness test showed a hardness of top part of sphere approximately 5 mN, which is relatively low. In addition, the thickness of sphere wall was calculated by interference method, it was from 0.1 to 1 microns.

It was discovered, that moisten alumina ceramics prone to formation of spherical structures from a melt after laser processing. During the laser ablation in near IR region, samples #1, #2, #5.2 and #6 produced the largest spheres up to 5 mm in diameter. During laser ablation in IR region, all samples were prone to be drilled though. It provided spheres on both (upper and bottom) surfaces. On the sample #1 were produced largest sphere up to 7 mm (570-810 W, 1-1.5 seconds of processing).

The significant melt expansion happened after the laser was switched off. It took 0.1-1s to grow completely. A melt bath behaved differently regarding the laser radiation regime. In cw

regime the bath was stable, while pulsed provided great fluctuations and sphere expansion between pulses.

LIST OF REFERENCES

Adelmann, B., Hellmann R. 2015. Rapid micro hole laser drilling in ceramic substrates using singlemode fiber laser. Journal of Materials Processing Technology, 221. Pp. 80–86.

Allegre, O.J., Perrie, W., Edwardson, S.P., Dearden, G. & Watkins, K.G. 2012. Laser microprocessing of steel with radially and azimuthally polarized femtosecond vortex pulses, 14. Pp. 1-9.

Bharatish, A., Narasimha Murthy, h.N., Anand, B., Madhusoodana, C.D., Praveena, G.S. & Krishna, M. 2013. Characterization of hole circularity and heat affected zone in pulsed CO2 laser drilling of alumina ceramics. Optics & Laser Technology, 53. Pp. 22-32.

Charee, W., Tangwarodomnukun, V. & Dumkum, C. 2016. Ultrasonic-assisted underwater laser micromachining of silicon. Journal of Materials Processing Technology, 231. Pp. 209-220.

Charee, W., Tangwarodomnukun, V. & Dumkum, C. 2014. Laser ablation of silicon in water under different flow rates. The International Journal of Advanced Manufacturing Technology, 78. Pp. 19-29.

Chen, M.-F., Hsiao, W.-Ts., Wang, M.-Ch., Yang, K.-Y. & Chen, Y.-F. 2015. A theoretical analysis and experimental verification of a laser drilling process for a ceramic substrate. The International Journal of Advanced Manufacturing Technology, 81. Pp. 1723–1732.

Cristoforetti, G., Legnaioli, S., Palleschi, V., Tognoni, E. & Benedetti, P.A. 2010. Crater drilling enhancement obtained in parallel non-collinear double-pulse laser ablation. Applied Physics A, , 98. Pp. 219-225.

Garcia-Giron, A., Sola, D., Pena, J.I. 2016. Liquid-assisted laser ablation of advanced ceramics and glass-ceramic materials. Applied Surface Science, 363. Pp. 548–554.

Genfu, Y., Wei, Zh., Xuehui, Ch. 2012. Contrast Test of KOH Solutions Jet- Assisted Laser Etching on Al2O3. Advanced Materials Research, 472-475. Pp. 2476-2479.

Hanon, M.M., Akman, E., Oztoprak, B.G., Gunes, M., Taha, Z.A., Hajim, K.I., Kacar, E., Gundogdu, O. & Demir, A. 2012. Experimental and theoretical investigation of the drilling of alumina ceramic using Nd:YAG pulsed laser. Optics & Laser Technology, 44. Pp. 913–922.

Iwatani, N., Doan, H.D. & Fushinobu, K. 2014. Optimization of near-infrared laser drilling of silicon carbide under water. International Journal of Heat and Mass Transfer, 71. Pp. 515–520.

Kacar, E., Mutlu, M., Akman, E., Demir, A., Candan, L., Canel, T., Gunay, V. & Sınmazcelik, T. 2009. Characterization of the drilling alumina ceramic using Nd:YAG pulsed laser. 209. Pp. 2008-2014.

Kraus, M., Ahmed, M.A., Michalowski, A., Voss, A., Weber, R. & Graf, Th. 2010. Microdrilling in steel using ultrashort pulsed laser beams with radial and azimuthal polarization. Optics Express, 18. Pp. 22305-22313.

Lee, Y.-Ch. & Cheng, M.-H. 2015. CO2 laser processing on ceramic substrates of light emitting diode assisted by compressed gas. Machining Science and Technology, 19. Pp. 400-415.

Li, D., Chen, X., Guo, Ch., Tian, J., Deng, Y. & Zhang, W. 2017. Micro surface texturing of alumina ceramic with nanosecond laser. Procedia Engineering, 174. Pp. 370-376.

Li, C., Shi, X., Si, J., Chen, T., Chen, F., Liang, Sh., Wu, Z. & Hou, X. 2009. Alcohol-assisted photoetching of silicon carbide with a femtosecond laser. Optics Communications, 282. Pp. 78-80.

Liu, Z., Gao, Y., Wu, B., Shen, N. & Ding, H. 2014. Ultrasound-assisted water-confined laser micromachining: a novel machining process., 2. Pp. 87-90.

Liu, Q., Zhang, L., Jiang, F., Liu, J., Cheng, L., Li, H. & Wang, Y. 2011. Laser ablation behaviors of SiC–ZrC coated carbon/carbon composites. Surface & Coatings Technology, 205. Pp. 4299–4303.

Lopez, J.M.L., Bakrania, A., Coupland, J. & Marimuthu, S. 2016. Droplet assisted laser micromachining of hard ceramics. Journal of the European Ceramic Society, 36. Pp. 2689–2694.

Lu¸ P. W. & Yuan, G. F. 2014. Experimental Study of Low-Pressure Water Jet Assisted Laser Drilling on Al2O3 Ceramic. Applied Mechanics and Materials, 599-601. Pp. 22-26.

Marti-Lopez, L., Ocana, R., Pineiro, E., Asensio, A. 2011. Laser Peening Induced Shock Waves and Cavitation Bubbles in Water Studied by Optical Schlieren Visualization. Physics Procedia, 12. Pp. 442–451.

Meier, M., Romano, V. & Feurer, T. 2007. Material processing with pulsed radially and azimuthally polarized laser radiation. Applied Physics A, 86. Pp. 329–334.

Mishra, S. & Yadava, V. 2015. Laser BeamMicroMachining(LBMM) – A review. Optics and Lasers in Engineering, 73. Pp. 89–122.

Ramoli, L., Khan, M.M.A. & Valentini, M. 2017. Through-the-thickness selective laser ablation of ceramic coatings on soda-lime glass. Optics & Laser Technology, 90. Pp. 113-121.

Nguyen, Th.T.Ph., Tanabe, R. & Ito, Y. 2014. Effects of an absorptive coating on the dynamics of underwater laser-induced shock process, 116. Pp. 1109–1117.

Samant, A.N. & Dahotre N.B. 2009. Laser machining of structural ceramics—A review. Journal of the European Ceramic Society, 29. Pp. 969–993.

Samant, A.N. & Dahotre N.B. 2010. Three-dimensional laser machining of structural ceramics. Journal of Manufacturing Processes, 12. Pp. 1-7.

Silvennoinen, M., Kaakkunen, J.J.J., Paivasaari, K. & Vahimaa, P. 2013. Water spray assisted ultrashort laser pulse ablation. Applied Surface Science, 265. Pp. 865– 869.

Sola, D., Escartin, A., Cases, R. & Pena, J. I. 2011. Laser ablation of advanced ceramics and glass-ceramic materials: Reference position dependence. Applied Surface Science, 257. Pp. 5413–5419.

Sinev, D.A., Dobrina, D.A., Strusevich, A.V., Veiko, V.P., Baranov M.A. & Yakusheva, A.A. 2016. Special regime of liquid-assisted laser ablation of ceramics. Applied Physics A, 122. Pp. 546.

Tangwarodomnukun, V., Wang, J., Huang, C.z. & Zhu, H.T. 2012. An investigation of hybrid laser–waterjet ablation of silicon substrates. International Journal of Machine Tools & Manufacture, 56. Pp. 39–49.

Tong, Y., Bai, Sh., Zhang, H., & Ye, Y. 2013. Laser ablation behavior and mechanism of C/SiC composite. Ceramics International, 39. Pp. 6813–6820.

Wang, H., Lin, H., Wang, Ch., Zheng, L. & Hu, X. 2017. Laser drilling of structural ceramics—A review. Journal of the European Ceramic Society, 37. Pp. 1157-1173.

Wang, L., Huang, Ch., Wang, J., Zhu, H. & Liang, X. 2018. An experimental investigation on laser assisted waterjet micro-milling of silicon nitride ceramics. Ceramics International, 44. Pp. 5636-5645.

Wee, L.M., Khoong, L.E., Tan, Ch.W & Lim, G.Ch. 2011. Solvent-Assisted Laser Drilling of Silicon Carbide. Applied Ceramic Technology, 8. Pp. 1263-1276.

Wee, L.M., Ng, E.Y.K., Prathama, A.H. & Zheng, H. 2011. Micro-machining of silicon wafer in air and under water. Optics & Laser Technology, 43. Pp. 62–71.

Xu, J.Y., Hu, H. & Lei, Y.L. 2014. Morphological features of silicon substrate by using different frequency laser ablation in air and water, 317. Pp. 666-671.

Yan, Z. & Chrisey, D.B. 2012. Pulsed laser ablation in liquid for micro-/nanostructure generation. Journal of Photochemistry and Photobiology C: Photochemistry Reviews, 13. Pp. 204– 223.

Yan, Y., Li, L., Sezer, K., Wang, W., Whitehead, D., Ji, L., Bao, Y. & Jiang, Y. 2011. CO2 laser underwater machining of deep cavities in alumina. Journal of the European Ceramic Society, 31. Pp. 2793–2807.

Yang, Y., Chen, Zh. & Zhang, Y. 2016. Melt flow and heat transfer in laser drilling. International Journal of Thermal Sciences, 107. Pp. 141-152.

Yang, Y., Yu, J., Cui, Y. & Huang, J., 2012. New laser machining technology of Al2O3 ceramic with complex shape. Ceramics International, 38. Pp. 3643–3648.